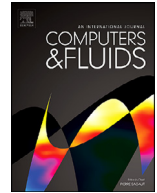




ELSEVIER

Contents lists available at ScienceDirect

Computers and Fluids

journal homepage: www.elsevier.com/locate/complfluid

Development of accurate and robust genuinely two-dimensional HLL-type Riemann solver for compressible flows

Lijun Hu^{a,*}, Li Yuan^{b,c}, Kunlei Zhao^{b,c}^a School of Mathematics and Statistics, Hengyang Normal University, Hunan 421002, China^b ICMSEC and LSEC, Academy of Mathematics and Systems Science, Chinese Academy of Sciences, Beijing 100190, China^c School of Mathematical Sciences, University of Chinese Academy of Sciences, Beijing 100190, China

ARTICLE INFO

Article history:

Received 10 May 2020

Revised 11 August 2020

Accepted 14 August 2020

Available online 18 September 2020

Keywords:

Euler equations

HLL-type Riemann solver

Genuinely two-dimensional

Zha-Bilgen splitting

Carbuncle phenomenon

Shock instability

ABSTRACT

When using the conventional direction splitting method to calculate multidimensional high speed gas-dynamical flows, Riemann solvers capable of resolving contact surface and shear wave accurately will suffer from different forms of shock instability, such as the notorious carbuncle phenomenon. The stability analysis shows that the lack of dissipation in the direction transverse to the shock front leads to the shock instability of low-dissipation HLEM solver. To overcome this defect, an accurate and carbuncle-free genuinely two-dimensional HLL-type Riemann solver is proposed. Using Zha-Bilgen splitting method, the flux vector of two-dimensional Euler equations is split into the convective flux and pressure flux. An algorithm similar to AUSM+ scheme is adopted to calculate the convective flux and the pressure flux is calculated by the low-dissipation HLEM scheme. Following Balsara's idea, the genuinely two-dimensional properties of the new solver are achieved by solving the two-dimensional Riemann problem that considers transversal features of the flow at each vertex of the cell interface. Numerical results of benchmark tests demonstrate that the new solver has higher resolution and better robustness than the conventional HLEM solver implemented in dimension by dimension.

© 2020 Elsevier Ltd. All rights reserved.

1. Introduction

At present, the Godunov-type numerical method based on approximate Riemann solvers has been widely used in simulations of compressible flows in both research and engineering applications. Some renowned Riemann solvers include Roe [1], HLL [2], HLLC [3], HLEM [4], HLLC [5] and AUSM-family schemes [6–9], etc. Among them, the HLL-type Riemann solvers are favored by many researchers due to their advantages in calculations, such as simplicity, positivity, entropy satisfying property and so on [10]. Although almost all HLL-type schemes can satisfactorily capture non-linear waves, shock wave or rarefaction wave, they can be divided into two categories according to their ability to resolve linear waves. The incomplete-wave HLL-type solvers, including HLL, HLLC, HLL-CPS [11], HLLC and HLLS [12], omit one or both of these linear waves and thus are incapable of resolving contact discontinuity or shear wave. The complete-wave HLL-type Riemann solvers, including HLEM, HLLC, HLLC+ [13], HLLI [14], are capable of resolving contact wave and shear wave and thus can accurately cal-

culate flow problems involving shear-dominated phenomena, vortices, flame fronts, material interfaces, mixing layers, etc [10].

Nevertheless, when calculating multidimensional strong shock wave problems these complete-wave HLL-type Riemann solvers will suffer from different forms of shock instability, including the infamous carbuncle phenomenon. Some attempts to save these low-dissipation HLL-type schemes from shock anomalies include hybridizations with dissipative schemes [15–18], dissipation-controlling technologies [10,12], selective wave modification method [19], artificial viscosity method [20,21], addition of shear viscosity [22], normal velocity reconstruction strategy [23], etc. These strategies have successfully cured the shock instability by increasing the numerical dissipation of the original schemes. However, they should be used with caution in calculations since the numerical dissipation out of place could sacrifice the accuracy for contact surface and shear layer.

In calculations of multidimensional problems, these conventional low-dissipation schemes implemented in dimension by dimension only consider the waves travelling orthogonal to the cell interface and fail to provide sufficient crossflow dissipation to dampen the perturbations that trigger the shock instability. Thus, constructing the genuinely multidimensional Riemann solvers that also consider the waves transverse to the cell interface has become

* Corresponding author.

E-mail addresses: hulijun@lsec.cc.ac.cn (L. Hu), lyuan@lsec.cc.ac.cn (L. Yuan), klzhao@lsec.cc.ac.cn (K. Zhao).

a good strategy to improve the resolution and robustness of numerical schemes [24,25]. Early attempts include the introduction of multidimensionality into one-dimensional solvers [26,27], corner transport method by Collella [24], Leveque's multidimensional wave propagation algorithm [28], weighted average flux method proposed by Billet and Toro [29], Wendroff's HLLC solver for multidimensional hypersonic conservative laws [30], multidimensional linearized Roe schemes by Fey [31] and Brio [25]. Although these multidimensional schemes exhibit some advantages over the conventional one-dimensional schemes, they do not enjoy great popularity in practice due to their mathematical complexity and thus unsatisfactory computational efficiency.

Recently, Balsara [32] proposes a genuinely two-dimensional HLLC solver which is simple and easy to implement due to its closed form. The multidimensionality of the solver is achieved by defining and solving a two-dimensional Riemann problem at each vertex of the cell interface. A three-dimensional version is also proposed later by the author in [33]. In order to restore the contact wave omitted by the multidimensional HLLC solver, Balsara [34] proposes a genuinely two-dimensional HLLC solver capable of resolving contact wave accurately by following the conventional one-dimensional HLLC scheme. To avoid specifying the direction of contact discontinuity in calculations, Balsara later constructs the multidimensional Riemann solver with self-similarity variables to solve hyperbolic conservation laws [35,36]. Following Balsara's idea, Gallardo et al. adopt the AVM (Approximate Viscosity Matrix) method to construct a class of genuinely two-dimensional incomplete-wave Riemann solvers and apply them to the numerical simulations of magnetohydrodynamic flows [37]. Adopting Zha-Bilgen convective-pressure flux splitting method [38], Mandal and Sharma [39] propose a two-dimensional HLL-CPS scheme and the version in curvilinear coordinates is implemented successfully by Qu et al. [40]. The genuinely two-dimensional HLL-CPS solvers based on Toro-Vázquez convective-pressure flux splitting method are developed in Cartesian coordinates [41] and curvilinear coordinates [42]. These multidimensional HLL-CPS Riemann solvers based on convective-pressure flux splitting method are simple and inexpensive but their capabilities to resolve shear wave should be further improved due to the incomplete wave structure of HLL-CPS scheme.

In this paper, an accurate and carbuncle-free genuinely two-dimensional HLLC Riemann solver based on Zha-Bilgen splitting procedure, called GT-HLLC-Z, is proposed. The convective flux is calculated by an algorithm similar to AUSM+ scheme and the pressure flux is calculated by the complete-wave HLLC solver. Following Balsara's idea, the two-dimensional Riemann problem that considers the transversal features of the flow at each vertex of the cell interface is solved to achieve the multidimensionality. The outline of the paper is as follows. After some preliminaries in Section 2, the capability of two HLL-type Riemann solvers to capture inviscid shear wave is investigated in Section 3. In Section 4, the stability analysis to explore the causes of shock instability is conducted. Section 5 introduces the construction of a genuinely two-dimensional HLLC Riemann solver. The results of several numerical tests are presented in Section 6. Finally, the conclusions are drawn in Section 7.

2. Preliminaries

The two-dimensional Euler equations that describe inviscid compressible flows can be expressed as

$$\frac{\partial \mathbf{U}}{\partial t} + \frac{\partial \mathbf{F}(\mathbf{U})}{\partial x} + \frac{\partial \mathbf{G}(\mathbf{U})}{\partial y} = \mathbf{0}, \quad (2.1)$$

with

$$\mathbf{U} = \begin{bmatrix} \rho \\ \rho u \\ \rho v \\ E \end{bmatrix}, \quad \mathbf{F}(\mathbf{U}) = \begin{bmatrix} \rho u \\ \rho u^2 + p \\ \rho uv \\ u(E + p) \end{bmatrix}, \quad \mathbf{G}(\mathbf{U}) = \begin{bmatrix} \rho v \\ \rho uv \\ \rho v^2 + p \\ v(E + p) \end{bmatrix}, \quad (2.2)$$

where ρ , u , v , p and E denote density, x -velocity, y -velocity, pressure and total energy. The system is closed through the equation of state for ideal gas

$$p = (\gamma - 1) \left[E - \frac{1}{2} \rho (u^2 + v^2) \right], \quad (2.3)$$

where the specific heat ratio $\gamma = 1.4$.

2.1. Finite volume discretization

The integral form of (2.1) is

$$\frac{d}{dt} \int_{\Omega} \mathbf{U} d\Omega + \oint_{\partial\Omega} [(\mathbf{F}, \mathbf{G}) \cdot \mathbf{n}] dl = \mathbf{0}, \quad (2.4)$$

where Ω denotes a control volume bounded by $\partial\Omega$, dl denotes an infinitesimal line element on $\partial\Omega$ and \mathbf{n} is the outward unit normal vector to $\partial\Omega$.

Using the uniform Cartesian grid with mesh spacings Δx and Δy to partition the computational domain, the finite volume discretization for (2.4) can be written as

$$\frac{d\mathbf{U}_{i,j}}{dt} = -\frac{1}{\Delta x} (\mathbf{F}_{i+1/2,j} - \mathbf{F}_{i-1/2,j}) - \frac{1}{\Delta y} (\mathbf{G}_{i,j+1/2} - \mathbf{G}_{i,j-1/2}), \quad (2.5)$$

where $\mathbf{U}_{i,j}$ is the volume-averaged value of \mathbf{U} , $\mathbf{F}_{i+1/2,j}$ and $\mathbf{F}_{i-1/2,j}$ denote numerical fluxes at cell interfaces $(i + 1/2, j)$ and $(i - 1/2, j)$, $\mathbf{G}_{i,j+1/2}$ and $\mathbf{G}_{i,j-1/2}$ are numerical fluxes at cell interfaces $(i, j + 1/2)$ and $(i, j - 1/2)$. In the following, the flux functions of two HLL-type Riemann solvers are reviewed in brief.

2.2. HLLC solver

Einfeldt et al. [4] propose a complete-wave HLLC solver that is capable of capturing contact discontinuity and shear wave. The flux function is as follows

$$\mathbf{F}_{1/2} = \frac{S_R \mathbf{F}_L - S_L \mathbf{F}_R}{S_R - S_L} + \frac{S_L S_R}{S_R - S_L} (\mathbf{U}_R - \mathbf{U}_L - \delta_2 \alpha_2 \mathbf{R}_2 - \delta_3 \alpha_3 \mathbf{R}_3), \quad (2.6)$$

where S_L and S_R are the smallest and largest wave speeds, $\mathbf{R}_{2,3}$ denote the right eigenvectors corresponding to linear degenerate fields, $\alpha_{2,3}$ denote the wave strengths and $\delta_{2,3}$ are coefficients to control the amount of dissipation. Their expressions are as follows

$$\begin{aligned} S_L &= \min(0, u_L - a_L, \tilde{u} - \tilde{a}), & S_R &= \max(0, u_R + a_R, \tilde{u} + \tilde{a}), \\ \mathbf{R}_2 &= \begin{bmatrix} 1 \\ \tilde{u} \\ \tilde{v} \\ \frac{\tilde{u}^2 + \tilde{v}^2}{2} \end{bmatrix}, & \mathbf{R}_3 &= \begin{bmatrix} 0 \\ 0 \\ 1 \\ \tilde{v} \end{bmatrix}, \\ \alpha_2 &= \Delta \rho - \frac{\Delta p}{\tilde{a}^2}, & \alpha_3 &= \tilde{\rho} \Delta v, \\ \delta_2 &= \delta_3 = \frac{\tilde{a}}{\tilde{a} + |\tilde{u}|}, \end{aligned} \quad (2.7)$$

where $\Delta(\cdot) = (\cdot)_R - (\cdot)_L$ and the Roe's averaged variables $\tilde{(\cdot)}$ are given by Roe [1],

$$\begin{aligned} \tilde{\rho} &= \sqrt{\rho_L \rho_R}, \\ \tilde{u} &= \frac{\sqrt{\rho_L} u_L + \sqrt{\rho_R} u_R}{\sqrt{\rho_L} + \sqrt{\rho_R}}, \\ \tilde{v} &= \frac{\sqrt{\rho_L} v_L + \sqrt{\rho_R} v_R}{\sqrt{\rho_L} + \sqrt{\rho_R}}, \end{aligned}$$

$$\tilde{H} = \frac{\sqrt{\rho_L}H_L + \sqrt{\rho_R}H_R}{\sqrt{\rho_L} + \sqrt{\rho_R}},$$

$$\tilde{a} = \sqrt{(\gamma - 1)\left[\tilde{H} - \frac{1}{2}(\tilde{u}^2 + \tilde{v}^2)\right]}, \quad (2.8)$$

with $H = (E + p)/\rho$ being the total enthalpy.

2.3. HLL-CPS solver

Mandal and Panwar [11] propose a new incomplete-wave HLL-CPS Riemann solver based on convective-pressure splitting method. Adopting Zha-Bilgen splitting procedure [38], the flux vector is split into convective flux and pressure flux as follows

$$\mathbf{F}(\mathbf{U}) = \begin{bmatrix} \rho u \\ \rho u^2 + p \\ \rho uv \\ u(E + p) \end{bmatrix} = \begin{bmatrix} \rho u \\ \rho u^2 \\ \rho uv \\ uE \end{bmatrix} + \begin{bmatrix} 0 \\ p \\ 0 \\ up \end{bmatrix} = \mathbf{F}_1 + \mathbf{F}_2. \quad (2.9)$$

The convective flux of the HLL-CPS solver is evaluated as follows

$$\mathbf{F}_{1(1/2)} = M_* \begin{bmatrix} \rho \\ \rho u \\ \rho v \\ E \end{bmatrix}_k a_*, \quad (2.10)$$

where

$$M_* = \begin{cases} \frac{\tilde{u}}{\tilde{u} - S_L} & \text{if } \tilde{u} \geq 0, \\ \frac{\tilde{u}}{\tilde{u} - S_R} & \text{if } \tilde{u} < 0, \end{cases} \quad (2.11)$$

$$a_* = \begin{cases} u_L - S_L & \text{if } \tilde{u} \geq 0, \\ u_R - S_R & \text{if } \tilde{u} < 0, \end{cases} \quad (2.12)$$

and

$$k = \begin{cases} L & \text{if } \tilde{u} \geq 0, \\ R & \text{if } \tilde{u} < 0, \end{cases} \quad (2.13)$$

with $\tilde{u} = (u_L + u_R)/2$.

The pressure flux of the HLL-CPS solver is evaluated based on HLL solver but using the isentropic condition $\tilde{a}^2 = \delta p/\delta \rho$, the density difference in the numerical diffusive term is replaced with the pressure difference for resolving contact discontinuity. The pressure flux can be expressed as

$$\mathbf{F}_{2(1/2)} = \frac{1}{2}(\mathbf{F}_{2L} + \mathbf{F}_{2R}) + \delta \mathbf{U}_2, \quad (2.14)$$

where

$$\delta \mathbf{U}_2 = \frac{S_R + S_L}{2(S_R - S_L)}(\mathbf{F}_{2L} - \mathbf{F}_{2R}) - \frac{S_L S_R}{\tilde{a}^2(S_R - S_L)} \begin{bmatrix} p_L - p_R \\ (pu)_L - (pu)_R \\ (pv)_L - (pv)_R \\ \frac{\tilde{a}^2}{\gamma - 1}(p_L - p_R) + \frac{1}{2}[(pu^2 + pv^2)_L - (pu^2 + pv^2)_R] \end{bmatrix}. \quad (2.15)$$

The choices of wave speeds S_L and S_R are the same as HLL solver, defined in (2.7). Thus, the total flux of HLL-CPS solver at a cell interface can be written as

$$\mathbf{F}_{1/2} = \mathbf{F}_{1(1/2)} + \frac{1}{2}(\mathbf{F}_{2L} + \mathbf{F}_{2R}) + \delta \mathbf{U}_2. \quad (2.16)$$

3. Numerical dissipation analysis of HLL-type Riemann solvers

In this section, we discuss the ability of HLL-EM and HLL-CPS solvers for preserving inviscid contact since it is a prerequisite for accurate resolution of viscous flows. For this purpose, a simple two-dimensional inviscid shear wave model is set up, i.e.,

$$(\rho, u, v, p)_{KJ} = \begin{cases} (\rho_L, 0, v_L, p_0) & K = I, \\ (\rho_R, 0, v_R, p_0) & K = I + 1. \end{cases} \quad (3.1)$$

In order to investigate the dissipative property of HLL-EM and HLL-CPS solvers for this simple model problem, we rewrite the flux function into a form that shows dissipation term explicitly

$$\mathbf{F}_{1/2} = \frac{1}{2}(\mathbf{F}_L + \mathbf{F}_R) + \mathbf{D}_{1/2}, \quad (3.2)$$

where $\mathbf{D}_{1/2}$ denotes the numerical diffusion term.

3.1. Numerical dissipation of HLL-EM scheme

For the flux function of HLL-EM solver in (2.6), the numerical diffusion term $\mathbf{D}_{1/2}$ can be written as

$$\mathbf{D}_{1/2} = \frac{S_R + S_L}{2(S_R - S_L)}(\mathbf{F}_L - \mathbf{F}_R) + \frac{S_L S_R}{S_R - S_L}(\mathbf{U}_R - \mathbf{U}_L - \delta_2 \alpha_2 \mathbf{R}_2 - \delta_3 \alpha_3 \mathbf{R}_3). \quad (3.3)$$

For the model problem (3.1), we have

$$\mathbf{F}_L = \begin{bmatrix} 0 \\ p_0 \\ 0 \\ 0 \end{bmatrix} = \mathbf{F}_R, \quad \mathbf{U}_L = \begin{bmatrix} \rho_L \\ 0 \\ \rho_L v_L \\ \frac{p_0}{\gamma - 1} + \frac{1}{2} \rho_L v_L^2 \end{bmatrix}, \quad \mathbf{U}_R = \begin{bmatrix} \rho_R \\ 0 \\ \rho_R v_R \\ \frac{p_0}{\gamma - 1} + \frac{1}{2} \rho_R v_R^2 \end{bmatrix} \quad (3.4)$$

and

$$\delta_2 = \delta_3 = 1, \quad \alpha_2 = \Delta \rho, \quad \alpha_3 = \tilde{\rho} \Delta v, \quad \mathbf{R}_2 = \begin{bmatrix} 1 \\ 0 \\ \tilde{v} \\ \frac{\tilde{v}^2}{2} \end{bmatrix}, \quad \mathbf{R}_3 = \begin{bmatrix} 0 \\ 0 \\ 1 \\ \tilde{v} \end{bmatrix}. \quad (3.5)$$

Substituting (3.4) and (3.5) into (3.3), we obtain

$$\mathbf{D}_{1/2} = \frac{S_L S_R}{S_R - S_L} \begin{bmatrix} 0 \\ 0 \\ (\rho_R v_R - \rho_L v_L) - (\tilde{v} \Delta \rho + \tilde{\rho} \Delta v) \\ \frac{1}{2}(\rho_R v_R^2 - \rho_L v_L^2) - \frac{1}{2}(\tilde{v}^2 \Delta \rho + 2\tilde{\rho} \tilde{v} \Delta v) \end{bmatrix}. \quad (3.6)$$

Considering the definitions of Roe's averaged variables given by (2.8), we have

$$\begin{aligned} \tilde{v} \Delta \rho + \tilde{\rho} \Delta v &= \frac{\sqrt{\rho_L} v_L + \sqrt{\rho_R} v_R}{\sqrt{\rho_L} + \sqrt{\rho_R}} \cdot \Delta \rho + \sqrt{\rho_L \rho_R} \cdot \Delta v \\ &= \frac{(\sqrt{\rho_L} v_L + \sqrt{\rho_R} v_R)(\sqrt{\rho_R} - \sqrt{\rho_L})}{(\sqrt{\rho_L} + \sqrt{\rho_R})(\sqrt{\rho_R} - \sqrt{\rho_L})} \cdot \Delta \rho + \sqrt{\rho_L \rho_R} \cdot \Delta v \\ &= \frac{\rho_R v_R - \rho_L v_L - \sqrt{\rho_L \rho_R}(v_R - v_L)}{\Delta \rho} \cdot \Delta \rho + \sqrt{\rho_L \rho_R} \cdot \Delta v \\ &= \rho_R v_R - \rho_L v_L \end{aligned} \quad (3.7)$$

and

$$\begin{aligned} \rho_R v_R^2 - \rho_L v_L^2 &= (\sqrt{\rho_R} v_R + \sqrt{\rho_L} v_L)(\sqrt{\rho_R} v_R - \sqrt{\rho_L} v_L) \\ &= \frac{\sqrt{\rho_R} v_R + \sqrt{\rho_L} v_L}{\sqrt{\rho_L} + \sqrt{\rho_R}} (\sqrt{\rho_L} + \sqrt{\rho_R})(\sqrt{\rho_R} v_R - \sqrt{\rho_L} v_L) \\ &= \tilde{v}[\rho_R v_R - \rho_L v_L + \sqrt{\rho_L \rho_R}(v_R - v_L)] \\ &= \tilde{v}(\tilde{v} \Delta \rho + \tilde{\rho} \Delta v + \tilde{\rho} \Delta v) \\ &= \tilde{v}^2 \Delta \rho + 2\tilde{\rho} \tilde{v} \Delta v, \end{aligned} \quad (3.8)$$

then $\mathbf{D}_{1/2} = \mathbf{0}$ in (3.6) and thus HLLM solver can resolve this inviscid shear wave exactly.

3.2. Numerical dissipation of HLL-CPS scheme

For the flux function of HLL-CPS solver in (2.16), the numerical diffusion term $\mathbf{D}_{1/2}$ can be written as

$$\mathbf{D}_{1/2} = \frac{S_R + S_L}{2(S_R - S_L)} (\mathbf{F}_{2L} - \mathbf{F}_{2R}) - \frac{S_L S_R}{\bar{a}^2 (S_R - S_L)} \begin{bmatrix} p_L - p_R \\ (pu)_L - (pu)_R \\ (pv)_L - (pv)_R \\ \frac{\bar{a}^2}{\gamma-1} (p_L - p_R) + \frac{1}{2} [(pu)^2 + (pv)^2]_L - (pu^2 + pv^2)_R \end{bmatrix} \quad (3.9)$$

For the model problem (3.1), we have

$$\mathbf{F}_L = \begin{bmatrix} 0 \\ p_0 \\ 0 \\ 0 \end{bmatrix} = \mathbf{F}_R. \quad (3.10)$$

Substituting (3.10) and the initial distribution (3.1) into (3.9), we can obtain

$$\mathbf{D}_{1/2} = \frac{S_L S_R}{\bar{a}^2 (S_R - S_L)} \begin{bmatrix} 0 \\ 0 \\ p_0 (u_R - v_L) \\ \frac{1}{2} p_0 (v_R^2 - v_L^2) \end{bmatrix}, \quad (3.11)$$

then $\mathbf{D}_{1/2} \neq \mathbf{0}$ in (3.11) and thus HLL-CPS solver fails to capture this inviscid shear wave. Therefore, the genuinely two-dimensional Riemann solvers based on HLL-CPS method in [39–42] need to be further improved for the resolution of shear wave, which is also demonstrated by results of numerical experiment in Section 6.7.

4. Mechanism analysis of numerical shock instability

The above numerical dissipation analysis shows that the HLLM solver can capture contact discontinuity and shear wave accurately. However, the disgusting shock instability will occur when using it to calculate multidimensional strong shock wave problems. In what follows, the causes of shock instability in the HLLM scheme will be analyzed in depth.

4.1. Local stability analysis

The odd-even decoupling problem proposed by Quirk [15] is a benchmark test for robustness of numerical schemes and thus the capability to dampen perturbations with saw-tooth initial profile has become a standard for judging the shock stability of schemes. Different from analyses conducted in [10,12,15,43] where only the evolution patterns of perturbations in the transverse direction are discussed, the evolution patterns of perturbations in both streamwise and transverse directions are sought for in the present work.

Suppose at t^n , a plane uniform flow travels in the x -direction with velocity $u_0 = M_0 a_0$ while the velocity in the y -direction $v_0 = 0$, where M_0 and a_0 are Mach number and sound speed. The density and pressure of the fluid are ρ_0 and p_0 , respectively.

4.1.1. Evolution patterns of perturbations in the streamwise direction

Firstly, the perturbations with saw-tooth profile are introduced in the x -direction (streamwise direction). The perturbed flow field is set as

$$\begin{cases} (\rho, u, v, p)_{i-1,j} = (\rho_0, u_0, 0, p_0) - (\hat{\rho}^n, \hat{u}^n, \hat{v}^n, \hat{p}^n), \\ (\rho, u, v, p)_{i,j} = (\rho_0, u_0, 0, p_0) + (\hat{\rho}^n, \hat{u}^n, \hat{v}^n, \hat{p}^n), \\ (\rho, u, v, p)_{i+1,j} = (\rho_0, u_0, 0, p_0) - (\hat{\rho}^n, \hat{u}^n, \hat{v}^n, \hat{p}^n), \end{cases} \quad (4.1)$$

where $\hat{\rho}^n, \hat{u}^n, \hat{v}^n$ and \hat{p}^n are perturbation variables at t^n . Since there is no perturbation in the y -direction, both $\mathbf{G}_{i,j-1/2}$ and $\mathbf{G}_{i,j+1/2}$ are equal to zero. Using the forward Euler method to discretize time, then the semi-discrete Eq. (2.5) can be written as

$$\mathbf{U}_{i,j}^{n+1} = \mathbf{U}_{i,j}^n - \sigma_x (\mathbf{F}_{i+1/2,j} - \mathbf{F}_{i-1/2,j}), \quad (4.2)$$

where $\sigma_x = \Delta t / \Delta x$ and Δt is the time step.

Calculating numerical fluxes $\mathbf{F}_{i-1/2,j}$ and $\mathbf{F}_{i+1/2,j}$ with the HLLM solver and substituting them into (4.2), the evolution patterns of perturbation variables can be obtained.

In the case of supersonic condition ($M_0 > 1$), the evolutionary equations of perturbation variables are as follows

$$\begin{bmatrix} \hat{\rho} \\ \hat{u} \\ \hat{v} \\ \hat{p} \end{bmatrix}^{n+1} = \begin{pmatrix} 1 - 2\sigma_x u_0 & -2\sigma_x \rho_0 & 0 & 0 \\ 0 & 1 - 2\sigma_x u_0 & 0 & -\frac{2\sigma_x}{\rho_0} \\ 0 & 0 & 1 - 2\sigma_x u_0 & 0 \\ 0 & -2\sigma_x \rho_0 a_0^2 & 0 & 1 - 2\sigma_x u_0 \end{pmatrix} \begin{bmatrix} \hat{\rho} \\ \hat{u} \\ \hat{v} \\ \hat{p} \end{bmatrix}^n \quad (4.3)$$

The eigenvalues of the amplification matrix in (4.3) are

$$\begin{aligned} \lambda_1^{\text{sup}} &= 1 - 2\sigma_x u_0, & \lambda_2^{\text{sup}} &= 1 - 2\sigma_x (u_0 + a_0), \\ \lambda_3^{\text{sup}} &= 1 - 2\sigma_x u_0, & \lambda_4^{\text{sup}} &= 1 - 2\sigma_x (u_0 - a_0). \end{aligned} \quad (4.4)$$

Eq. (4.4) indicates that $|\lambda_i^{\text{sup}}| < 1$ ($i = 1, 2, 3, 4$) and thus each perturbation variable can be effectively damped if $\sigma_x < 1/(u_0 + a_0)$.

In the case of subsonic condition ($0 < M_0 < 1$), the evolutionary equations of perturbation variables are as follows

$$\begin{bmatrix} \hat{\rho} \\ \hat{u} \\ \hat{v} \\ \hat{p} \end{bmatrix}^{n+1} = \begin{pmatrix} 1 - 2\sigma_x u_0 & -\frac{2\sigma_x \rho_0 u_0}{a_0} & 0 & \frac{2\sigma_x (u_0 - a_0)}{a_0^2} \\ 0 & 1 - 2\sigma_x a_0 & 0 & -\frac{2\sigma_x u_0}{\rho_0 a_0} \\ 0 & 0 & 1 - 2\sigma_x u_0 & 0 \\ 0 & -2\sigma_x \rho_0 u_0 a_0 & 0 & 1 - 2\sigma_x a_0 \end{pmatrix} \begin{bmatrix} \hat{\rho} \\ \hat{u} \\ \hat{v} \\ \hat{p} \end{bmatrix}^n \quad (4.5)$$

The eigenvalues of the amplification matrix in (4.5) are

$$\begin{aligned} \lambda_1^{\text{sub}} &= 1 - 2\sigma_x u_0, & \lambda_2^{\text{sub}} &= 1 - 2\sigma_x (a_0 + u_0), \\ \lambda_3^{\text{sub}} &= 1 - 2\sigma_x u_0, & \lambda_4^{\text{sub}} &= 1 - 2\sigma_x (a_0 - u_0). \end{aligned} \quad (4.6)$$

Eq. (4.6) indicates that $|\lambda_i^{\text{sub}}| < 1$ ($i = 1, 2, 3, 4$) and each perturbation variable can be effectively damped if $\sigma_x < 1/(a_0 + u_0)$.

4.1.2. Evolution patterns of perturbations in the transverse direction

The perturbations with saw-tooth profile are introduced in the y -direction (transverse direction) and the perturbed flow field is set as

$$\begin{cases} (\rho, u, v, p)_{i,j-1} = (\rho_0, u_0, 0, p_0) - (\hat{\rho}^n, \hat{u}^n, \hat{v}^n, \hat{p}^n), \\ (\rho, u, v, p)_{i,j} = (\rho_0, u_0, 0, p_0) + (\hat{\rho}^n, \hat{u}^n, \hat{v}^n, \hat{p}^n), \\ (\rho, u, v, p)_{i,j+1} = (\rho_0, u_0, 0, p_0) - (\hat{\rho}^n, \hat{u}^n, \hat{v}^n, \hat{p}^n). \end{cases} \quad (4.7)$$

Since there is no perturbation in the x -direction, both $\mathbf{F}_{i-1/2,j}$ and $\mathbf{F}_{i+1/2,j}$ are equal to zero. After time discretization, the semi-discrete Eq. (2.5) becomes

$$\mathbf{U}_{i,j}^{n+1} = \mathbf{U}_{i,j}^n - \sigma_y (\mathbf{G}_{i,j+1/2} - \mathbf{G}_{i,j-1/2}), \quad (4.8)$$

where $\sigma_y = \Delta t / \Delta y$.

Calculating numerical fluxes $\mathbf{G}_{i,j-1/2}$ and $\mathbf{G}_{i,j+1/2}$ with HLLM solver and substituting them into (4.8), then the evolutionary equations of perturbation variables are as follows

$$\begin{bmatrix} \hat{\rho} \\ \hat{u} \\ \hat{v} \\ \hat{p} \end{bmatrix}^{n+1} = \begin{pmatrix} 1 & 0 & 0 & -\frac{2\sigma_y}{a_0} \\ 0 & 1 & 0 & 0 \\ 0 & 0 & 1 - 2\sigma_y a_0 & 0 \\ 0 & 0 & 0 & 1 - 2\sigma_y a_0 \end{pmatrix} \begin{bmatrix} \hat{\rho} \\ \hat{u} \\ \hat{v} \\ \hat{p} \end{bmatrix}^n \quad (4.9)$$

The eigenvalues of the amplification matrix in (4.9) are

$$\lambda_1 = \lambda_2 = 1, \quad \lambda_3 = \lambda_4 = 1 - 2\sigma_y a_0. \quad (4.10)$$

Eq. (4.10) indicates that \hat{v} and \hat{p} can be damped effectively if $\sigma_y < 1/a_0$ while $\hat{\rho}$ and \hat{u} will not be damped since their amplification factors are equal to 1.0 for any σ_y .

To sum up, all perturbations in the streamwise direction can be effectively damped but perturbations of density and shear velocity in the transverse direction will not be damped. These accumulated errors in the transverse direction will trigger the shock instability and ultimately destroy the calculation of strong shock waves.

4.2. Global stability analysis

The above local stability analysis is based on a uniform flow that does not involve the shock wave and only considers the evolution of perturbations at a local cell. To reflect the effect of shock wave and consider the evolution of perturbations in the whole flow field, a global stability analysis of the HLLEM scheme for a steady standing shock is carried out.

4.2.1. Steady standing shock problem

The domain $[0, 1] \times [0, 1]$ is covered by 20×20 uniform Cartesian grid. A steady standing shock with Mach number $M_0 = 7$ is located at the cell interfaces shared by the tenth and eleventh columns. The upstream states of the shock are given as

$$\mathbf{U}_{(0)} = \left(1, 1, 0, \frac{1}{\gamma(\gamma-1)M_0^2} + \frac{1}{2} \right)^T \tag{4.11}$$

and the downstream states are obtained through the Rankine-Hugoniot relations

$$\begin{aligned} \mathbf{U}_{(1)} &= \left(f(M_0), 1, 0, \frac{g(M_0)}{\gamma(\gamma-1)M_0^2} + \frac{1}{2f(M_0)} \right)^T, \\ f(M_0) &= \left(\frac{2}{\gamma+1} \frac{1}{M_0^2} + \frac{\gamma-1}{\gamma+1} \right)^{-1}, \\ g(M_0) &= \frac{2\gamma}{\gamma+1} M_0^2 - \frac{\gamma-1}{\gamma+1}. \end{aligned} \tag{4.12}$$

The following random perturbations are introduced into the entire flow field through conserved variables

$$\hat{\mathbf{U}}_{i,j}^0 = (1 + \alpha_{i,j} \cdot 10^{-7}) \mathbf{U}_{i,j}^0, \tag{4.13}$$

where $\hat{\mathbf{U}}_{i,j}^0$ is the vector of perturbed conserved variables, $\mathbf{U}_{i,j}^0$ is the initial states given by (4.11) and (4.12), $\alpha_{i,j}$ is a random number between 0 and 1. The exact upstream and downstream conditions are imposed at the left and right boundaries, and the periodic boundary conditions are used for the top and bottom. In what follows, a global matrix-based stability analysis for this steady standing shock with random perturbations is implemented.

4.2.2. Global matrix-based stability analysis

The implementation procedure of the matrix-based stability analysis method is described detailedly in the creative paper by Dumbser et al. [44]. Here we give a brief introduction for convenience. The flow field given by (4.13) can be rewritten as the following form

$$\mathbf{U}_m = \mathbf{U}_m^0 + \delta \mathbf{U}_m, \tag{4.14}$$

where \mathbf{U}_m^0 and $\delta \mathbf{U}_m$ denote the steady mean value and the error, respectively, the subscript m represents the global cell index. The flux function at the interface shared by cells with index m and k can be linearized as follows

$$\Phi_{mk}(\mathbf{U}_m, \mathbf{U}_k) = \Phi_{mk}(\mathbf{U}_m^0, \mathbf{U}_k^0) + \frac{\partial \Phi_{mk}}{\partial \mathbf{U}_m} \delta \mathbf{U}_m + \frac{\partial \Phi_{mk}}{\partial \mathbf{U}_k} \delta \mathbf{U}_k. \tag{4.15}$$

Substituting the linearized flux function (4.15) into the integral form (2.4) of Euler equations, we can obtain the evolution equations of the error

$$\frac{d(\delta \mathbf{U}_m)}{dt} = -\frac{1}{|\Omega_m|} \sum_{\Gamma_{mk} \subset \partial \Omega_m} |\Gamma_{mk}| \left[\frac{\partial \Phi_{mk}}{\partial \mathbf{U}_m} \delta \mathbf{U}_m + \frac{\partial \Phi_{mk}}{\partial \mathbf{U}_k} \delta \mathbf{U}_k \right], \tag{4.16}$$

where $|\Omega_m|$ is the area of cell Ω_m and $|\Gamma_{mk}|$ is the length of cell interface Γ_{mk} . The matrix form of (4.16) is as follows

$$\frac{d}{dt} \begin{bmatrix} \delta \mathbf{U}_1 \\ \vdots \\ \delta \mathbf{U}_q \end{bmatrix} = \mathbf{S} \begin{bmatrix} \delta \mathbf{U}_1 \\ \vdots \\ \delta \mathbf{U}_q \end{bmatrix}, \tag{4.17}$$

where $q = 20 \times 20$ is the total number of cells, \mathbf{S} denotes the stability matrix. Solving Eq. (4.17), we can obtain the evolutionary equations of initial errors

$$\begin{bmatrix} \delta \mathbf{U}_1 \\ \vdots \\ \delta \mathbf{U}_q \end{bmatrix} (t) = e^{\mathbf{S}t} \begin{bmatrix} \delta \mathbf{U}_1 \\ \vdots \\ \delta \mathbf{U}_q \end{bmatrix}_{t=0} \tag{4.18}$$

which is bounded if

$$\max(\text{Re}(\lambda(\mathbf{S}))) \leq 0, \tag{4.19}$$

where $\text{Re}(\lambda(\mathbf{S}))$ represents the real part of eigenvalues of the stability matrix \mathbf{S} .

Fig. 4.1 shows the distribution of eigenvalues of the stability matrix \mathbf{S} in a complex plane. The maximum value of the real part of eigenvalues obtained from the HLLEM solver is 14.9204, which is corresponding to a destabilized solution. If the transverse flux is replaced by the dissipative HLL flux but the longitudinal flux is still calculated by the HLLEM scheme, a stable solution will be obtained. However, it is worth noting that if the longitudinal flux is replaced by the HLL flux and the HLLEM flux is used in the transverse direction, it still gives an unstable pattern. The density profiles shown in Fig. 4.2 also illustrate that the insufficiency of transverse dissipation in the HLLEM solver leads to the occurrence of shock instability.

5. Genuinely Two-dimensional HLLEM solver based on Zha-Bilgen splitting procedure (GT-HLLEM-Z)

A local cell (i, j) and its neighbors in 2D Cartesian grid are shown in Fig. 5.1(a). The conventional direction splitting method only considers the one-dimensional flux at the midpoint of a cell interface involving states L (Left) and R (Right), but Balsara's genuinely two-dimensional framework also considers the flux at each vertex of a cell interface [32]. For example, there is a two-dimensional Riemann problem at vertex C_1 where four states (named as LU, LD, RU, RD) interact with each other and the solution of this Riemann problem contributes the genuinely two-dimensional flux. The evolution of this two-dimensional Riemann problem with time is shown in Fig. 5.1(b), where S_L, S_R, S_U and S_D are the fastest 'left', 'right' 'up' and 'down' moving waves whose definitions are given in Section 5.3.3. In this paper, $\mathbf{F}_{i+1/2,j}$ and $\mathbf{G}_{i,j+1/2}$ denote numerical fluxes in the x - and y -directions at the midpoint of the cell interface, $\mathbf{F}_{i+1/2,j+1/2}$ and $\mathbf{G}_{i+1/2,j+1/2}$ represent numerical fluxes in the x - and y -directions at the vertex of the cell interface.

5.1. Zha-Bilgen splitting

Zha and Bilgen [38] split the flux vector of Euler equations into convective part and pressure part as follows

$$\mathbf{F}(\mathbf{U}) = \begin{bmatrix} \rho u \\ \rho u^2 \\ \rho uv \\ uE \end{bmatrix} + \begin{bmatrix} 0 \\ p \\ 0 \\ pu \end{bmatrix} = \mathbf{F}^c + \mathbf{F}^p. \tag{5.1}$$

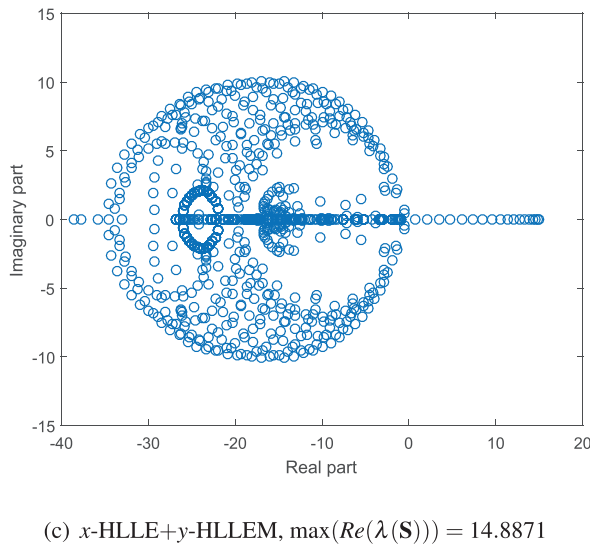
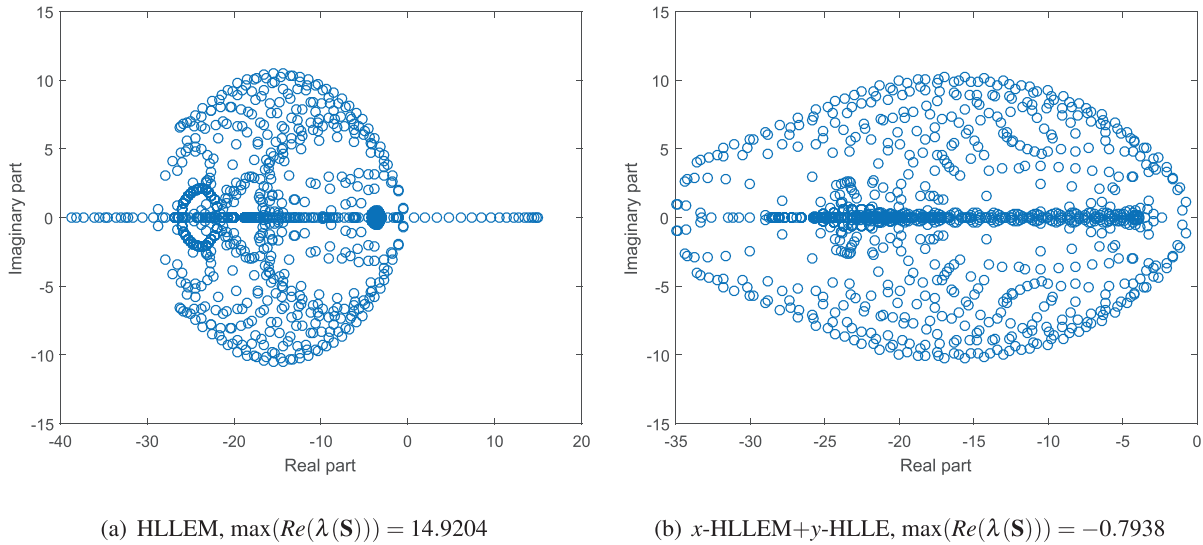


Fig. 4.1. Distribution of eigenvalues of the stability matrix \mathbf{S} in complex plane.

The Jacobian matrix of convective flux \mathbf{F}^c is

$$\mathbf{M} = \begin{pmatrix} 0 & 1 & 0 & 0 \\ -u^2 & 2u & 0 & 0 \\ -uv & v & u & 0 \\ -\frac{uE}{\rho} & \frac{E}{\rho} & 0 & u \end{pmatrix}. \tag{5.2}$$

Four eigenvalues of \mathbf{M} are as follows

$$\lambda_1^c = \lambda_2^c = \lambda_3^c = \lambda_4^c = u. \tag{5.3}$$

The Jacobian matrix of pressure flux \mathbf{F}^p is

$$\mathbf{N} = \begin{pmatrix} 0 & 0 & 0 & 0 \\ \frac{\gamma-1}{2}(u^2 + v^2) & -(\gamma-1)u & -(\gamma-1)v & \gamma-1 \\ 0 & 0 & 0 & 0 \\ (\gamma-1)u(u^2 + v^2 - \frac{E}{\rho}) & (\gamma-1)(\frac{E}{\rho} - \frac{3}{2}u^2 - \frac{1}{2}v^2) & -(\gamma-1)uv & (\gamma-1)u \end{pmatrix}. \tag{5.4}$$

Four eigenvalues of \mathbf{N} are as follows

$$\lambda_1^p = -a\sqrt{\frac{\gamma-1}{\gamma}}, \quad \lambda_2^p = \lambda_3^p = 0, \quad \lambda_4^p = a\sqrt{\frac{\gamma-1}{\gamma}}, \tag{5.5}$$

where $a = \sqrt{\gamma p / \rho}$ is the local speed of sound.

5.2. Calculation of interface flux at the midpoint

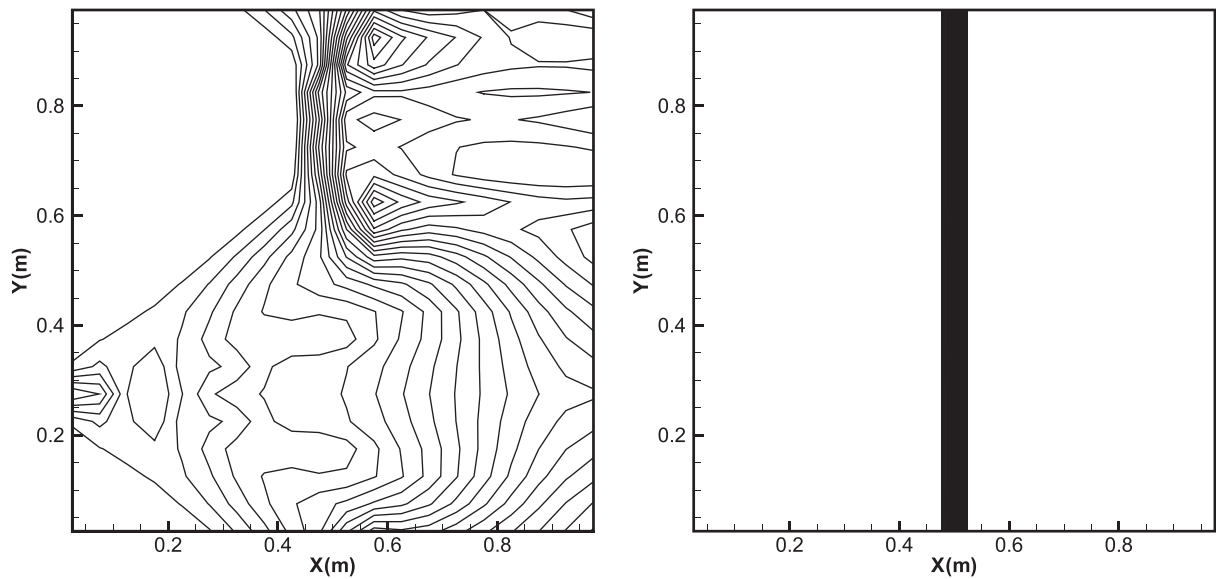
After Zha-Bilgen splitting procedure, the interface flux at the midpoint can be written as

$$\mathbf{F}_{i+1/2,j} = \mathbf{F}_{i+1/2,j}^c + \mathbf{F}_{i+1/2,j}^p, \quad \mathbf{G}_{i,j+1/2} = \mathbf{G}_{i,j+1/2}^c + \mathbf{G}_{i,j+1/2}^p. \tag{5.6}$$

5.2.1. Calculation of convective flux at the midpoint

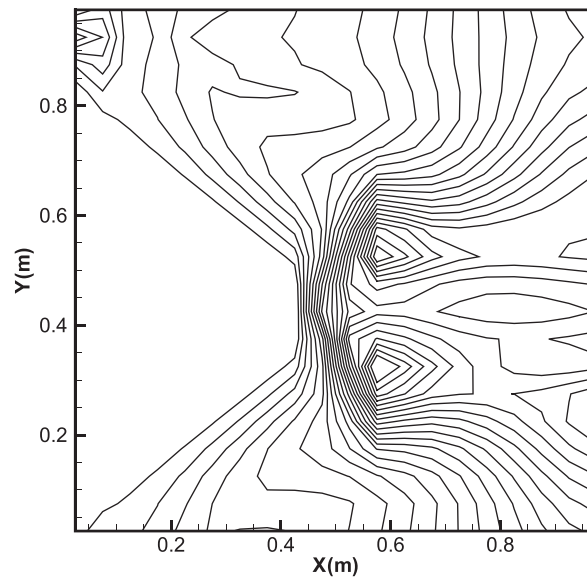
The upwind method similar to AUSM+ [6] scheme is adopted to calculate the convective flux at the midpoint

$$\mathbf{F}_{i+1/2,j}^c = M_{1/2} \begin{bmatrix} \rho a \\ \rho au \\ \rho av \\ aE \end{bmatrix}_k, \tag{5.7}$$



(a) HLEM

(b) x-HLEM+y-HLLE



(c) x-HLLE+y-HLEM

Fig. 4.2. Density profiles of two-dimensional steady standing shock with random perturbations at $t = 10$.

$$M_{1/2} = M_L^+ + M_R^-, \tag{5.8}$$

and

$$M^\pm = \begin{cases} \pm \frac{1}{4} (M \pm 1)^2 \pm \frac{1}{8} (M^2 - 1)^2 & \text{if } |M| \leq 1, \\ \frac{1}{2} (M \pm |M|) & \text{if } |M| > 1, \end{cases} \tag{5.9}$$

where $M = u/a$ is Mach number. The subscript k denoting the state selected for upwinding is given as

$$k = \begin{cases} L & \text{if } M_{1/2} \geq 0, \\ R & \text{if } M_{1/2} < 0. \end{cases} \tag{5.10}$$

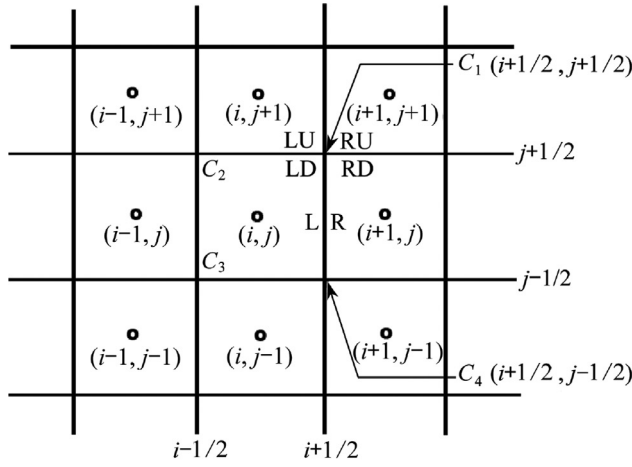
5.2.2. Calculation of pressure flux at the midpoint

An algorithm similar to the conventional HLEM solver is used to calculate the pressure flux at the midpoint

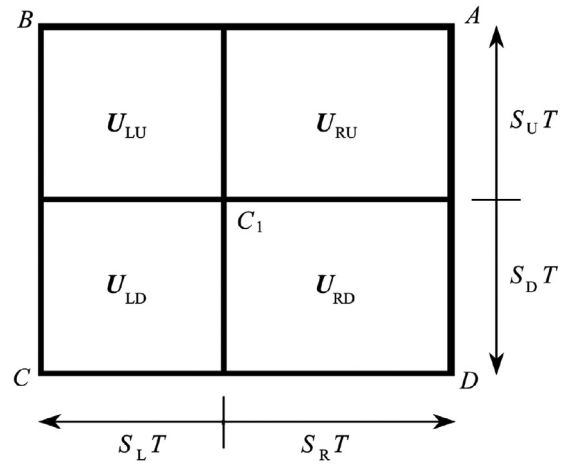
$$\mathbf{F}_{i+1/2,j}^p = \frac{S_R^M \mathbf{F}_L^p - S_L^M \mathbf{F}_R^p}{S_R^M - S_L^M} + \frac{S_L^M S_R^M}{S_R^M - S_L^M} (\mathbf{U}_R - \mathbf{U}_L - \delta_2 \alpha_2 \mathbf{R}_2 - \delta_3 \alpha_3 \mathbf{R}_3). \tag{5.11}$$

The expressions of $\delta_{2,3}$, $\alpha_{2,3}$ and $\mathbf{R}_{2,3}$ are given in (2.7). The wave speeds S_L^M and S_R^M are selected according to the conventional HLEM scheme

$$S_L^M = \min(0, u_L - a_L, \tilde{u} - \tilde{a}), \quad S_R^M = \max(0, u_R + a_R, \tilde{u} + \tilde{a}). \tag{5.12}$$



(a) Cell (i, j) and its neighbors



(b) 2D Riemann problem at vertex C_1

Fig. 5.1. Two-dimensional Cartesian grid and the wave model for the 2D Riemann problem at a vertex.

5.3. Calculation of flux at the vertex of cell interface

After Zha-Bilgen splitting procedure, the fluxes at the vertex of cell interface can be written as

$$\begin{aligned} \mathbf{F}_{i+1/2, j+1/2} &= \mathbf{F}_{i+1/2, j+1/2}^c + \mathbf{F}_{i+1/2, j+1/2}^p, \\ \mathbf{G}_{i+1/2, j+1/2} &= \mathbf{G}_{i+1/2, j+1/2}^c + \mathbf{G}_{i+1/2, j+1/2}^p. \end{aligned} \quad (5.13)$$

5.3.1. Calculation of convective flux at the vertex

An algorithm similar to AUSM+ scheme is also used to calculate the convective flux at the vertex and the influence of waves from transverse cells is also considered. Take the x-flux as example,

$$\mathbf{F}_{i+1/2, j+1/2}^c = \bar{M}_x \frac{S_U \begin{bmatrix} \rho a \\ \rho a u \\ \rho a v \\ a E \end{bmatrix}_{k_1} - S_D \begin{bmatrix} \rho a \\ \rho a u \\ \rho a v \\ a E \end{bmatrix}_{k_2}}{S_U - S_D}, \quad (5.14)$$

with

$$\bar{M}_x = \bar{M}_L^+ + \bar{M}_R^-, \quad (5.15)$$

$$\bar{M}^\pm = \begin{cases} \pm \frac{1}{4}(\bar{M} \pm 1)^2 \pm \frac{1}{8}(\bar{M}^2 - 1)^2 & \text{if } |\bar{M}| \leq 1, \\ \frac{1}{2}(\bar{M} \pm |\bar{M}|) & \text{if } |\bar{M}| > 1, \end{cases} \quad (5.16)$$

where

$$\bar{M}_L = \frac{\bar{u}_L}{\bar{a}_L}, \quad \bar{M}_R = \frac{\bar{u}_R}{\bar{a}_R}, \quad (5.17)$$

$$\bar{u}_L = \frac{u_{LU} S_U - u_{LD} S_D}{S_U - S_D}, \quad \bar{u}_R = \frac{u_{RU} S_U - u_{RD} S_D}{S_U - S_D}, \quad (5.18)$$

$$\bar{a}_L = \frac{a_{LU} S_U - a_{LD} S_D}{S_U - S_D}, \quad \bar{a}_R = \frac{a_{RU} S_U - a_{RD} S_D}{S_U - S_D}. \quad (5.19)$$

Subscripts k_1 and k_2 denoting the states selected for upwinding are given as follows

$$\begin{cases} k_1 = LU, k_2 = LD & \text{if } \bar{M}_x \geq 0, \\ k_1 = RU, k_2 = RD & \text{if } \bar{M}_x < 0. \end{cases} \quad (5.20)$$

Similarly, the convective flux in the y-direction at the vertex is calculated as follows

$$\mathbf{G}_{i+1/2, j+1/2}^c = \bar{M}_y \frac{S_R \begin{bmatrix} \rho a \\ \rho a u \\ \rho a v \\ a E \end{bmatrix}_{k_1} - S_L \begin{bmatrix} \rho a \\ \rho a u \\ \rho a v \\ a E \end{bmatrix}_{k_2}}{S_R - S_L}, \quad (5.21)$$

with

$$\bar{M}_y = \bar{M}_D^+ + \bar{M}_U^-, \quad (5.22)$$

$$\bar{M}^\pm = \begin{cases} \pm \frac{1}{4}(\bar{M} \pm 1)^2 \pm \frac{1}{8}(\bar{M}^2 - 1)^2 & \text{if } |\bar{M}| \leq 1, \\ \frac{1}{2}(\bar{M} \pm |\bar{M}|) & \text{if } |\bar{M}| > 1, \end{cases} \quad (5.23)$$

where

$$\bar{M}_D = \frac{\bar{v}_D}{\bar{a}_D}, \quad \bar{M}_U = \frac{\bar{v}_U}{\bar{a}_U}, \quad (5.24)$$

$$\bar{v}_D = \frac{v_{RD} S_R - v_{LD} S_L}{S_R - S_L}, \quad \bar{v}_U = \frac{v_{RU} S_R - v_{LU} S_L}{S_R - S_L}, \quad (5.25)$$

$$\bar{a}_D = \frac{a_{RD} S_R - a_{LD} S_L}{S_R - S_L}, \quad \bar{a}_U = \frac{a_{RU} S_R - a_{LU} S_L}{S_R - S_L}, \quad (5.26)$$

and

$$\begin{cases} k_1 = RD, k_2 = LD & \text{if } \bar{M}_y \geq 0, \\ k_1 = RU, k_2 = LU & \text{if } \bar{M}_y < 0. \end{cases} \quad (5.27)$$

5.3.2. Calculation of pressure flux at the vertex

Following ideas of genuinely two-dimensional HLL solver by Balsara [34] and AVM (Approximate Viscosity Matrix) solver by Gallardo et al. [37], a genuinely two-dimensional HLEM solver is proposed here to calculate the pressure flux at the vertex. Take the x-flux as example,

$$\begin{aligned} \mathbf{F}_{i+1/2, j+1/2}^p &= \frac{S_U}{S_U - S_D} \left(\frac{F_L^{p,*} + F_R^{p,*}}{2} - \frac{1}{2} (b_0 (\mathbf{U}_{RU} - \mathbf{U}_{LU} - \delta_2^U \alpha_2^U \mathbf{R}_2^U \right. \\ &\quad \left. - \delta_3^U \alpha_3^U \mathbf{R}_3^U) + b_1 (\mathbf{F}_R^{p,*} - \mathbf{F}_L^{p,*})) \right) \\ &\quad - \frac{S_D}{S_U - S_D} \left(\frac{F_L^{p,*} + F_R^{p,*}}{2} - \frac{1}{2} (b_0 (\mathbf{U}_{RD} - \mathbf{U}_{LD} - \delta_2^D \alpha_2^D \mathbf{R}_2^D \right. \\ &\quad \left. - \delta_3^D \alpha_3^D \mathbf{R}_3^D) + b_1 (\mathbf{F}_R^{p,*} - \mathbf{F}_L^{p,*})) \right) \\ &\quad + \frac{b_0}{2(S_U - S_D)} (\mathbf{G}_{RU}^p - \mathbf{G}_{LU}^p + \mathbf{G}_{LD}^p - \mathbf{G}_{RD}^p), \end{aligned} \quad (5.28)$$

where $\delta_{2,3}^U$, $\alpha_{2,3}^U$ and $\mathbf{R}_{2,3}^U$ that denote dissipation-controlling coefficients, wave strengths and right eigenvectors corresponding to linear degenerate fields are calculated between states \mathbf{U}_{LU} and \mathbf{U}_{RU} , $\delta_{2,3}^D$, $\alpha_{2,3}^D$ and $\mathbf{R}_{2,3}^D$ are calculated between states \mathbf{U}_{LD} and \mathbf{U}_{RD} . Coefficients b_0 and b_1 are given as

$$b_0 = -2 \frac{S_L S_R}{S_R - S_L}, \quad b_1 = \frac{S_R + S_L}{S_R - S_L}. \quad (5.29)$$

The essential three steps in calculations of transverse fluxes $\mathbf{F}_\beta^{p,*}$ ($\beta = L, R$) are as follows

(1) Calculate the resolved states \mathbf{U}_β^* between states $\mathbf{U}_{\beta D}$ and $\mathbf{U}_{\beta U}$

$$\mathbf{U}_\beta^* = \frac{S_U \mathbf{U}_{\beta U} - S_D \mathbf{U}_{\beta D} + \mathbf{G}_{\beta D} - \mathbf{G}_{\beta U}}{S_U - S_D}. \quad (5.30)$$

(2) Calculate one-dimensional HLLM fluxes \mathbf{G}_β^* between states $\mathbf{U}_{\beta D}$ and $\mathbf{U}_{\beta U}$

$$\mathbf{G}_\beta^* = \frac{S_U \mathbf{G}_{\beta D} - S_D \mathbf{G}_{\beta U}}{S_U - S_D} + \frac{S_D S_U}{S_U - S_D} (\mathbf{U}_{\beta U} - \mathbf{U}_{\beta D} - \delta_2 \alpha_2 \mathbf{R}_2 - \delta_3 \alpha_3 \mathbf{R}_3). \quad (5.31)$$

(3) The required x -velocity u_β^* and pressure p_β^* for $\mathbf{F}_\beta^{p,*}$ are obtained as follows

$$u_\beta^* = \frac{\mathbf{G}_\beta^*(2)}{\mathbf{G}_\beta^*(1)}, \quad p_\beta^* = \mathbf{G}_\beta^*(3) - \mathbf{G}_\beta^*(1) \cdot \frac{\mathbf{U}_\beta^*(3)}{\mathbf{U}_\beta^*(1)}, \quad (5.32)$$

where $\mathbf{U}_\beta^*(k)$ and $\mathbf{G}_\beta^*(k)$ represent the k th components of \mathbf{U}_β^* and \mathbf{G}_β^* , respectively.

Similarly, the pressure flux in the y -direction at the vertex is calculated as follows

$$\begin{aligned} \mathbf{G}_{i+1/2,j+1/2}^p &= \frac{S_R}{S_R - S_L} \left(\frac{G_D^{p,*} + G_U^{p,*}}{2} - \frac{1}{2} (c_0 (\mathbf{U}_{RU} - \mathbf{U}_{RD} - \delta_2^R \alpha_2^R \mathbf{R}_2^R \right. \\ &\quad \left. - \delta_3^R \alpha_3^R \mathbf{R}_3^R) + c_1 (\mathbf{G}_U^{p,*} - \mathbf{G}_D^{p,*})) \right) \\ &\quad - \frac{S_L}{S_R - S_L} \left(\frac{G_D^{p,*} + G_U^{p,*}}{2} - \frac{1}{2} (c_0 (\mathbf{U}_{LU} - \mathbf{U}_{LD} - \delta_2^L \alpha_2^L \mathbf{R}_2^L \right. \\ &\quad \left. - \delta_3^L \alpha_3^L \mathbf{R}_3^L) + c_1 (\mathbf{G}_U^{p,*} - \mathbf{G}_D^{p,*})) \right) \\ &\quad + \frac{c_0}{2(S_R - S_L)} (\mathbf{F}_{RU}^p - \mathbf{F}_{LU}^p + \mathbf{F}_{LD}^p - \mathbf{F}_{RD}^p), \end{aligned} \quad (5.33)$$

where $\delta_{2,3}^R$, $\alpha_{2,3}^R$ and $\mathbf{R}_{2,3}^R$ are calculated between states \mathbf{U}_{RD} and \mathbf{U}_{RU} , $\delta_{2,3}^L$, $\alpha_{2,3}^L$ and $\mathbf{R}_{2,3}^L$ are calculated between states \mathbf{U}_{LD} and \mathbf{U}_{LU} . Coefficients c_0 and c_1 are given as

$$c_0 = -2 \frac{S_D S_U}{S_U - S_D}, \quad c_1 = \frac{S_U + S_D}{S_U - S_D}. \quad (5.34)$$

The mechanism analysis of shock instability in Section 4 demonstrates that the conventional HLLM solver implemented in dimension by dimension fails to provide sufficient dissipation in the direction transverse to the shock front to dampen perturbations and these perturbations will trigger the shock instability and produce the spurious solutions for multidimensional strong shock waves. By contrast, the flux of genuinely two-dimensional GT-HLLM-Z solver includes the contribution from transverse cells. For example, in (5.14) for the x -directional convective flux at the vertex, the average fluid velocity and sound speed defined in (5.18) and (5.19) consider the information from transverse cells. The pressure flux at the vertex of the GT-HLLM-Z solver also includes the contribution from transverse cells. For example, in (5.28) for the x -directional pressure flux at the vertex,

the pressure in $\mathbf{F}_\beta^{p,*}$ is from the transverse HLLM flux \mathbf{G}_β^* and the last term on the right hand side consists of cross derivative of transverse pressure flux \mathbf{G}_{RU}^p , \mathbf{G}_{LU}^p , \mathbf{G}_{LD}^p and \mathbf{G}_{RD}^p . Therefore, the genuinely two-dimensional GT-HLLM-Z solver can successfully suppress the shock instability by virtue of the effect from transversal waves, which is demonstrated later through a series of numerical experiments.

5.3.3. Selection of wave speeds for 2D Riemann problem at the vertex

With respect to wave speeds for calculating the convective flux and pressure flux at the vertex, the choices in [39] are adopted

$$\begin{aligned} S_L &= \min(0, \lambda_x^0(\mathbf{U}_{LU}), \lambda_x^0(\mathbf{U}_{LD}), \tilde{\lambda}_x^0(\mathbf{U}_{LU}, \mathbf{U}_{RU}), \tilde{\lambda}_x^0(\mathbf{U}_{LD}, \mathbf{U}_{RD})), \\ S_R &= \max(0, \lambda_x^1(\mathbf{U}_{RU}), \lambda_x^1(\mathbf{U}_{RD}), \tilde{\lambda}_x^1(\mathbf{U}_{LU}, \mathbf{U}_{RU}), \tilde{\lambda}_x^1(\mathbf{U}_{LD}, \mathbf{U}_{RD})), \\ S_D &= \min(0, \lambda_y^0(\mathbf{U}_{RD}), \lambda_y^0(\mathbf{U}_{LD}), \tilde{\lambda}_y^0(\mathbf{U}_{RD}, \mathbf{U}_{RU}), \tilde{\lambda}_y^0(\mathbf{U}_{LD}, \mathbf{U}_{LU})), \\ S_U &= \max(0, \lambda_y^1(\mathbf{U}_{RU}), \lambda_y^1(\mathbf{U}_{LU}), \tilde{\lambda}_y^1(\mathbf{U}_{RD}, \mathbf{U}_{RU}), \tilde{\lambda}_y^1(\mathbf{U}_{LD}, \mathbf{U}_{LU})), \end{aligned} \quad (5.35)$$

where,

$\lambda_x^0(\mathbf{U}_{LU})$ is the smallest x -directional wave speed calculated in state \mathbf{U}_{LU} ;

$\lambda_x^1(\mathbf{U}_{RU})$ is the largest x -directional wave speed calculated in state \mathbf{U}_{RU} ;

$\lambda_x^0(\mathbf{U}_{LU}, \mathbf{U}_{RU})$ is the smallest x -directional wave speed calculated in Roe averaged state between \mathbf{U}_{LU} and \mathbf{U}_{RU} ;

$\lambda_x^1(\mathbf{U}_{LU}, \mathbf{U}_{RU})$ is the largest x -directional wave speed calculated in Roe averaged state between \mathbf{U}_{LU} and \mathbf{U}_{RU} .

The remaining terms can be defined in a similar way.

5.4. Calculation of total normal flux at a cell interface

As shown in Fig. 5.1(a), the total normal flux through the cell interface ($i + 1/2, j$) consists of conventional one-dimensional flux at the midpoint and the x -directional two-dimensional fluxes at vertices $C_1(i + 1/2, j + 1/2)$ and $C_4(i + 1/2, j - 1/2)$. Simpson formula is used to assemble these three fluxes and obtain the total normal flux at the cell interface

$$\bar{\mathbf{F}}_{i+1/2,j} = \frac{1}{6} \mathbf{F}_{i+1/2,j+1/2} + \frac{4}{6} \mathbf{F}_{i+1/2,j} + \frac{1}{6} \mathbf{F}_{i+1/2,j-1/2}. \quad (5.36)$$

Similarly, the total normal flux through the cell interface ($i, j + 1/2$) is given by

$$\bar{\mathbf{G}}_{i,j+1/2} = \frac{1}{6} \mathbf{G}_{i+1/2,j+1/2} + \frac{4}{6} \mathbf{G}_{i,j+1/2} + \frac{1}{6} \mathbf{G}_{i-1/2,j+1/2}. \quad (5.37)$$

6. Numerical results

In this section, several multidimensional test problems are calculated to validate the accuracy and robustness of the new solver. Since the higher order accuracy can stabilize the shock to some extent [45], some test cases showing the improvement of robustness are calculated with plain first-order accuracy while others are calculated with second-order accuracy. In order to achieve the second-order accuracy, the solution dependent weighted least squares (SDWLS) reconstruction method [46] is implemented in space discretization and the second-order TVD Runge-Kutta method is implemented in time discretization. Unless specifically noted, the plain first-order accuracy is adopted.

6.1. Two-dimensional steady standing shock problem

A two-dimensional steady standing shock with Mach number $M = 7$ is calculated [47]. The computational domain $[0, 1] \times [0,$

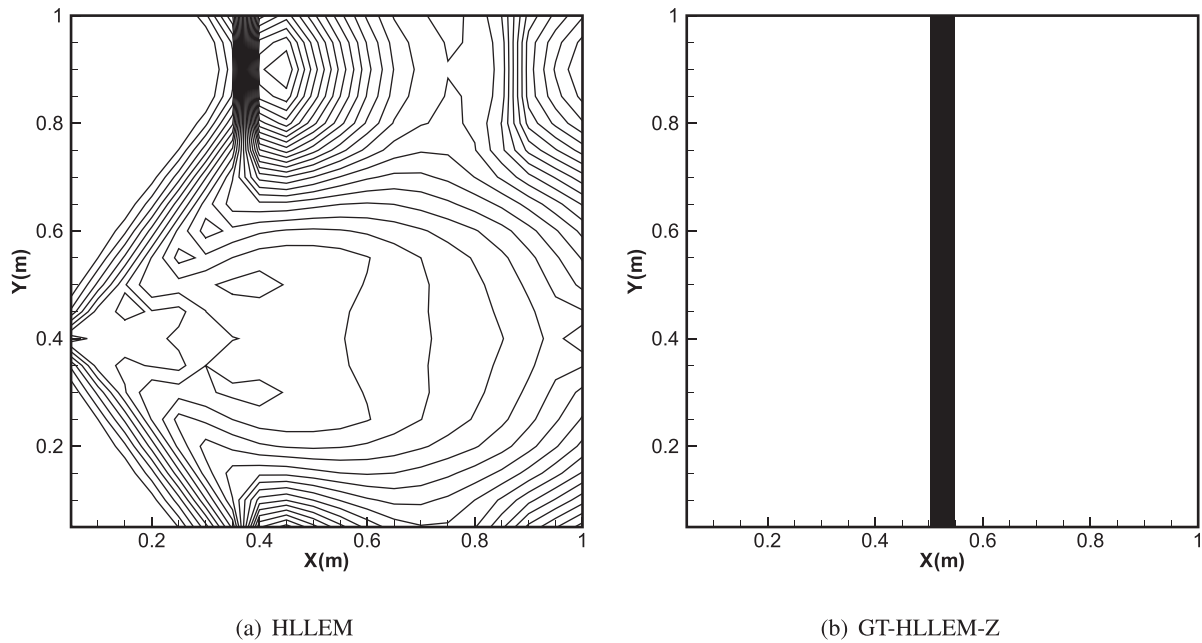


Fig. 6.1. Density profiles of Mach 7 two-dimensional steady standing shock.

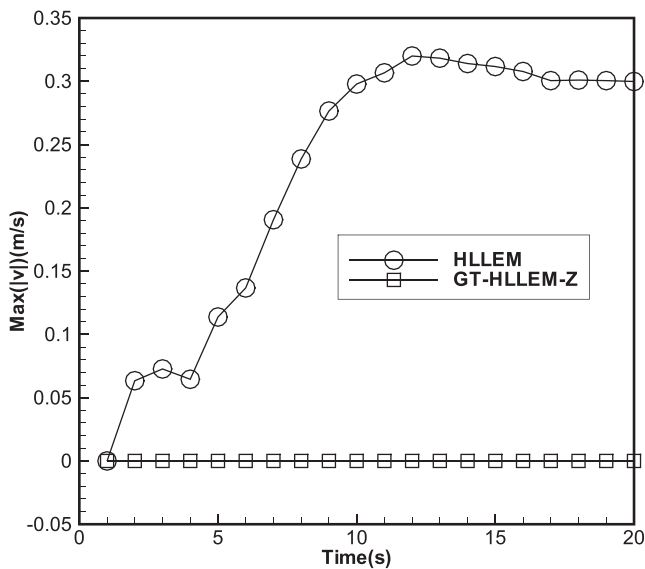


Fig. 6.2. Maximum magnitude of y-velocity of the steady standing shock problem.

1] is covered by 20×20 Cartesian grid and the standing shock is initially located at the cell interfaces shared by the tenth and eleventh columns. The initial states on the supersonic side are set as $(\rho, u, v, p)_L = (1, 1, 0, 0.014573)$ and the states on the subsonic side are $(\rho, u, v, p)_R = (5.44, 0.183673, 0, 0.830903)$. There is no perturbation on the initial conditions and the round-off errors act as the trigger for instability. The supersonic and subsonic conditions are imposed at the left and right boundaries while the top and bottom use the periodic boundary conditions. The density profiles at $t = 20$ are plotted in Fig. 6.1. The shock front given by HLEM solver is completely destroyed while the genuinely two-dimensional GT-HLEM-Z solver gives a stable solution with clean shock front. The destabilized behaviour of HLEM solver is also confirmed by the spurious tangential velocity v shown in Fig. 6.2.

6.2. Moving normal shock problem

A normal shock with Mach number 10 initially located at $x = 5$ propagates in a duct that covers a domain $[0, 1500] \times [0, 20]$. The uniform cells with mesh spacing $\Delta x = \Delta y = 1$ are adopted. The upstream conditions are set as $(\rho_0, u_0, v_0, p_0)_L = (1.4, 0, 0, 1)$ and the downstream conditions are given by the relation between shock wave and Mach number. Different from Quirk's moving normal shock problem [15] where the shock instability is triggered by the small perturbation of gridline, numerical random noise ranging from -0.5×10^{-6} to 0.5×10^{-6} is introduced into the initial upstream states while the gridline is free from any perturbation. The density profiles at $t = 150$ are plotted in Fig. 6.3. The conventional one-dimensional HLEM solver produces an unstable solution and the shock front is distorted completely while the genuinely two-dimensional GT-HLEM-Z solver eliminates the instability and obtains the clear shock front. The tangential velocities v shown in Fig. 6.4 also confirm the instability of HLEM scheme and the robustness of GT-HLEM-Z scheme.

6.3. Double Mach reflection problem

A well-known benchmark test problem called double Mach reflection problem is calculated to examine the robustness of the proposed scheme against shock anomalies. Woodward and Colella [48] formulate this problem and provide suitable initial conditions so that the problem can be simulated in a rectangular domain. A Mach 10 oblique shock, making a 60° angle with the bottom wall at $x = 1/6$, propagates through the domain $[0, 4] \times [0, 1]$. For the present test, 480×120 Cartesian grid is adopted. The initial conditions of the whole domain are set as

$$(\rho_0, u_0, v_0, p_0) = \begin{cases} (1.4, 0, 0, 1) & \text{if } y < \sqrt{3}(x - \frac{1}{6}), \\ (8, \frac{33\sqrt{3}}{8}, -4.125, 116.5) & \text{else.} \end{cases} \quad (6.1)$$

The post-shock conditions are maintained at the left boundary while all gradients are set to zero at the right boundary. The boundary conditions at the top are set to follow the propagation of the shock. As for the bottom, post-shock conditions are assigned

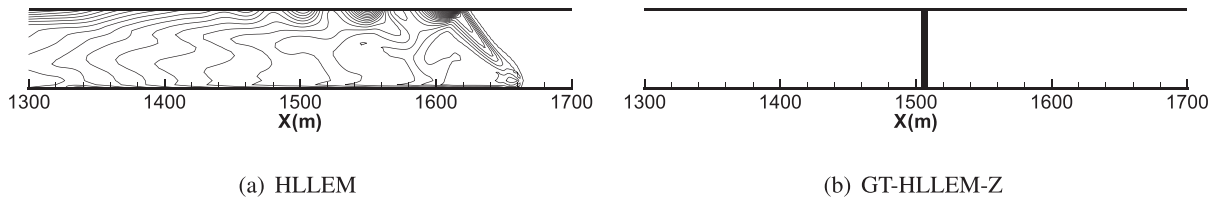


Fig. 6.3. Density profiles of Mach 10 moving normal shock.

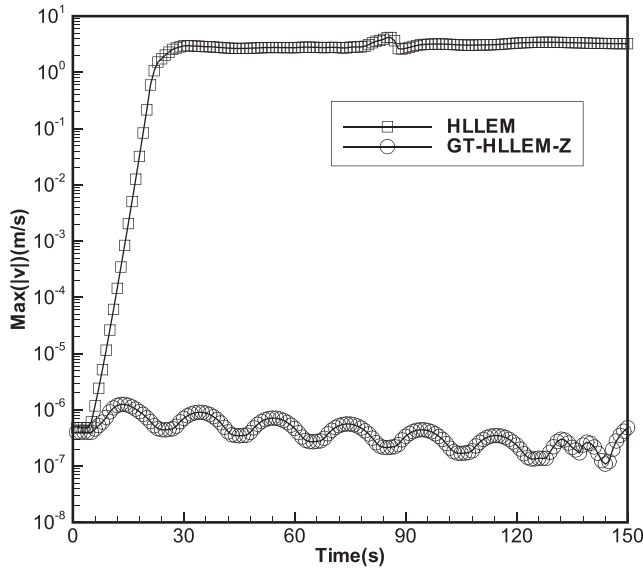


Fig. 6.4. Maximum magnitude of y -velocity of the moving normal shock problem.

from $x = 0$ to $x = 1/6$ while reflective conditions are adopted from $x = 1/6$ to $x = 4$. The density profiles of HLLM and GT-HLLM-Z solvers are displayed in Fig. 6.5. Like other complete-wave Riemann solvers, the conventional one-dimensional HLLM solver gives rise to severely kinked Mach stem and a spurious triple point while the GT-HLLM-Z solver eliminates these unphysical features and gives a solution without any instability. It is worth noting that the CFL number adopted by the conventional HLLM solver can not be more than 0.5 while the genuinely two-dimensional GT-HLLM-Z solver performs well with CFL number up to 0.9. This also confirms another advantage remarked in [32,37] that the genuinely two-dimensional schemes allow the use of a maximal CFL number of unity while the conventional solvers applied in dimension by dimension only allow the maximal CFL number of 0.5 [24,37]. Although the CPU time of the GT-HLLM-Z solver in a single timestep is about 1.89 times that of the HLLM solver, its computational efficiency is comparable to that of the one-dimensional HLLM

solver since it permits a larger CFL number and therefore larger timesteps.

6.4. 2D Sedov blast wave problem

A spherically symmetric explosion, known as Sedov blast wave problem, is calculated here to examine the robustness of GT-HLLM-Z solver in calculation of problems involving high pressure ratio and strong shock waves. The computational domain $[0, 2.4] \times [0, 2.4]$ is covered by 480×480 uniform cells. The initial conditions are set as $(\rho_0, u_0, v_0, p_0) = (1, 0, 0, 10^{-10})$ except the pressure of the central domain that consists of one cell in each of four quadrants is $3.5 \cdot 10^5$. All four boundaries adopt the reflective conditions. The pressure profiles of HLLM and GT-HLLM-Z solvers with second-order accuracy are shown in Fig. 6.6. Four visible carbuncles are produced by the conventional HLLM solver while the genuinely two-dimensional GT-HLLM-Z solver eliminates these unphysical carbuncles and gives a clear shock front. The CFL number adopted by the conventional HLLM solver can not be more than 0.4 but it can be up to 0.95 in GT-HLLM-Z solver.

6.5. Forward facing step problem

This problem, extensively studied by Woodward and Colella [48], involves a Mach 3 supersonic flow passing through a domain $[0, 3] \times [0, 1]$ including a step with the corner locating at $(x, y) = (0.6, 0.2)$. The 240×80 uniform Cartesian grid is adopted. The initial conditions of the whole domain are set as $(\rho_0, u_0, v_0, p_0) = (1.4, 3, 0, 1)$. The inflow conditions are imposed at the left boundary while the outlet conditions with all gradients vanishing are used at the right boundary. The top and bottom boundaries are inviscid walls where the reflective conditions are imposed. The density profiles of HLLM and GT-HLLM-Z solvers with second-order accuracy are shown in Fig. 6.7. The oscillations at the front of the step and the normal shock stem near the top are clearly visible in the solution obtained from the conventional HLLM scheme while the genuinely two-dimensional GT-HLLM-Z scheme eliminates the instability and produces a stable solution without any oscillation. The CFL number adopted by the conventional HLLM solver can not be more than 0.5 but it can be up to 0.9 in the GT-HLLM-Z solver.

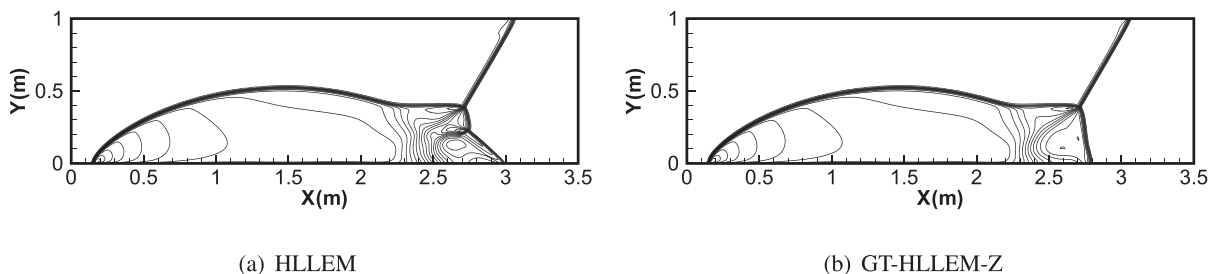


Fig. 6.5. Density profiles of the double Mach reflection problem at $t = 0.2$.

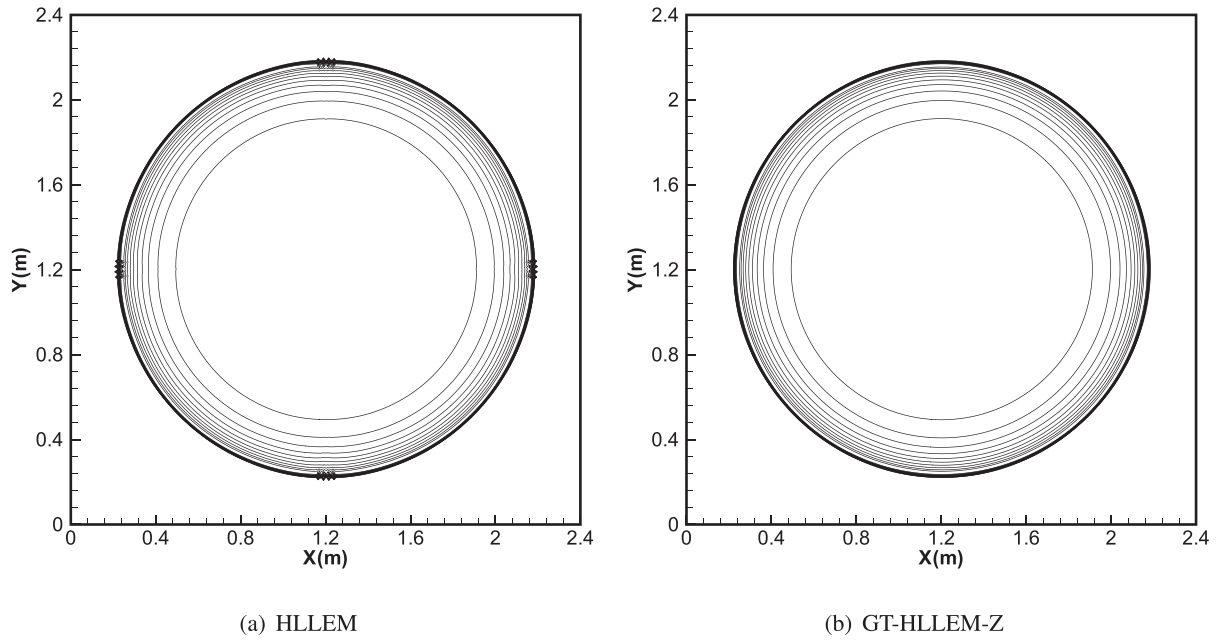


Fig. 6.6. Pressure profiles of the 2D Sedov blast wave problem at $t = 0.1$.

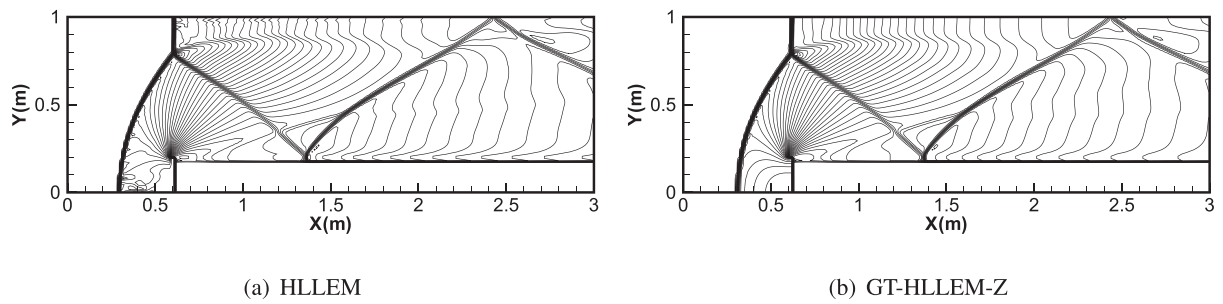


Fig. 6.7. Density profiles of the forward facing step problem at $t = 4$.

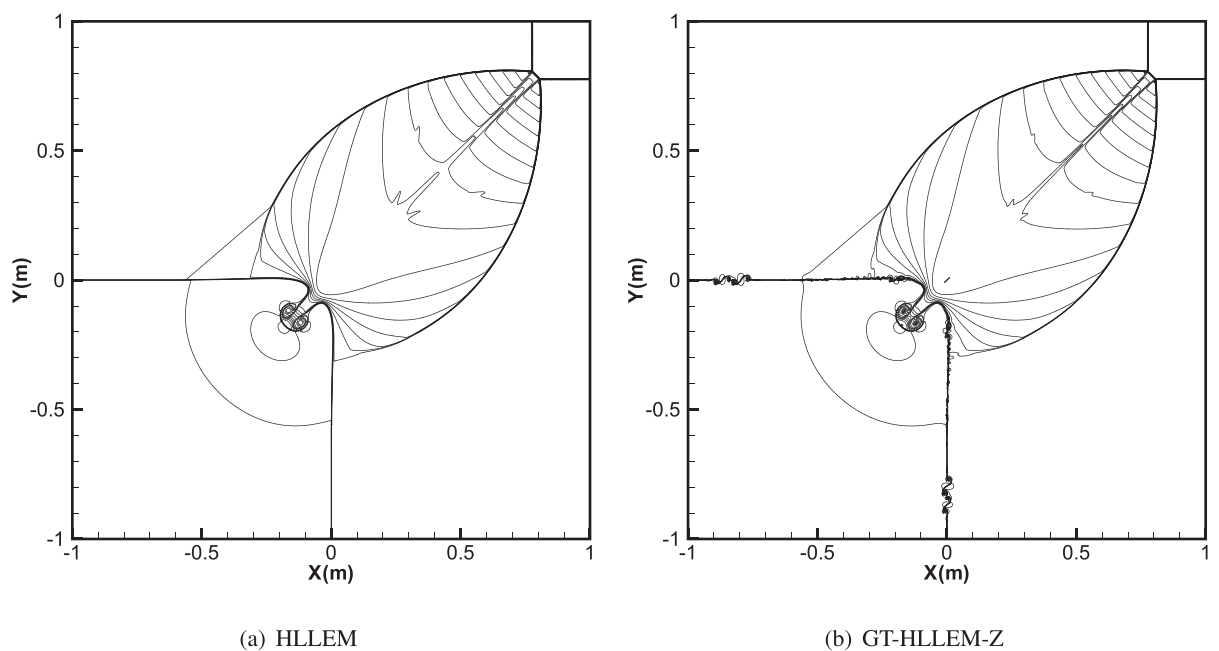


Fig. 6.8. Density profiles of the two-dimensional Riemann problem.

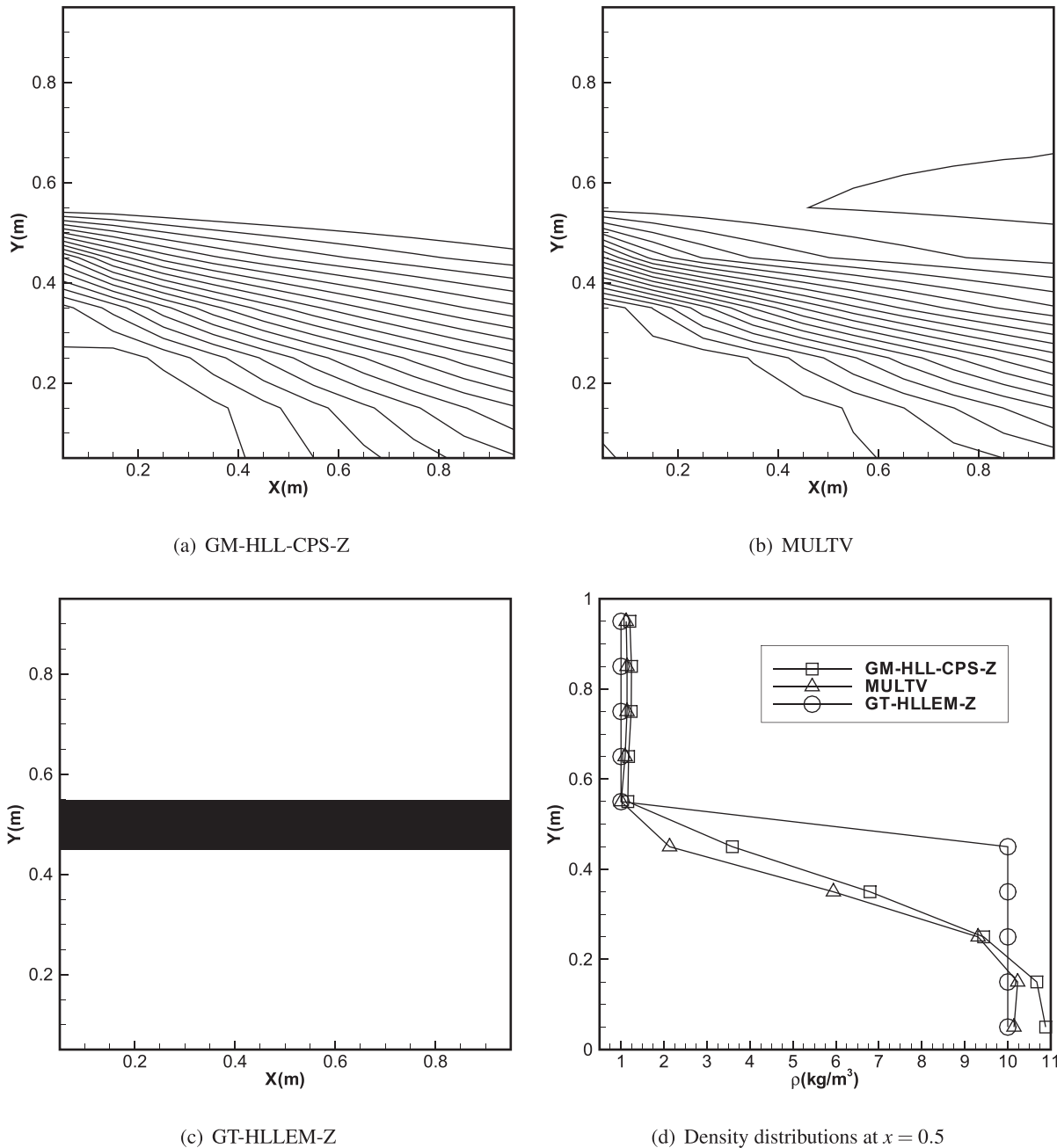


Fig. 6.9. Density profiles and the density distributions at $x = 0.5$ of the two-dimensional supersonic shear flow problem.

6.6. Two-dimensional Riemann problem

A two-dimensional Riemann problem described in [25] is calculated here to examine the resolution of the proposed solver. The computational domain $[-1, 1] \times [-1, 1]$ is partitioned into 2000×2000 uniform cells and the initial conditions are set as

$$(\rho_0, u_0, v_0, p_0) = \begin{cases} (0.5313, 0.0, 0.0, 0.4) & \text{if } x > 0, y > 0, \\ (1.0, 0.0, 0.7276, 1.0) & \text{if } x > 0, y < 0, \\ (1.0, 0.7276, 0.0, 1.0) & \text{if } x < 0, y > 0, \\ (0.8, 0.0, 0.0, 1.0) & \text{if } x < 0, y < 0. \end{cases} \quad (6.2)$$

Free-flow conditions are used at all four boundaries. The computation lasts until $t = 0.5$. The density profiles of HLLM and GT-HLLEM-Z solvers with second-order accuracy are shown in Fig. 6.8. It can be clearly observed that the genuinely two-dimensional GT-HLLEM-Z solver can resolve the flow features with greater details

and exhibits the visible Kelvin-Helmholtz instability roll-up as reported in [39,40] while the conventional one-dimensional HLLM solver fails to do so even on the finer grid of size 4000×4000 . The Kelvin-Helmholtz instability is caused by the discontinuity in the flow field and it can be regarded as valid and accurate solutions to the Euler equations [49]. So this test case highlights the higher resolution afforded by the genuinely two-dimensional GT-HLLEM-Z solver over the conventional one-dimensional solver. The CFL number adopted by the conventional HLLM solver can not be more than 0.5 but it can be up to 0.95 in the GT-HLLEM-Z solver.

6.7. Two-dimensional supersonic shear flow problem

This test case is calculated to examine the capability of a given scheme to capture the inviscid shear wave. It is an invaluable property for accurately resolving the shear layer in calculations of vis-

ous flows. The computational domain $[0, 1] \times [0, 1]$ is covered by 20×20 uniform cells and the initial conditions of two fluids in the upper and lower parts of the domain are set as

$$(\rho_0, u_0, v_0, p_0) = \begin{cases} (1, 2\sqrt{1.4}, 0, 1) & \text{if } y > 0.5, \\ (10, \frac{\sqrt{16.94}}{10}, 0, 1) & \text{if } y \leq 0.5. \end{cases} \quad (6.3)$$

Fig. 6.9 shows the density profiles and the density distribution at $x = 0.5$ after 1000 iterations. As analyzed in Section 3.2, two genuinely two-dimensional schemes based on HLL-CPS solver, i.e., GM-HLL-CPS-Z [39] and MULTV [42], fail to preserve the shear wave while the present GT-HLLEM-Z solver can capture it exactly.

7. Conclusions

This work proposes a genuinely two-dimensional HLLEM Riemann solver based on Zha-Bilgen splitting procedure. Using Zha-Bilgen splitting method, the flux vector of two-dimensional Euler equations is split into two parts, the convective flux and the pressure flux. An algorithm similar to AUSM+ scheme is used to calculate the convective flux and the pressure flux is calculated by the low-dissipation HLLEM scheme. Following Balsara's idea, the multidimensionality of the new solver is achieved by solving a two-dimensional Riemann problem involving four states at each vertex of the cell interface and thus the total flux through a cell interface is constructed by assembling a one-dimensional flux at the middle point with two genuinely two-dimensional fluxes at vertices. Stability analysis shows that the genuinely two-dimensional flux at the vertex that consider transversal features of the flow can effectively suppress the shock anomalies in the vicinity of strong shock waves. The performance of the new solver has been assessed in a number of test problems. The calculations of several strong shock wave problems fully demonstrate the robustness of the new solver and the capability to capture the Kelvin-Helmholtz instability in the 2D Riemann problem also indicates its higher resolution than the conventional HLLEM solver implemented in dimension by dimension. The capability of the new solver to accurately resolve contact discontinuities and shear waves makes it very suitable for calculating viscous flow problems. In addition, numerical experiments also confirm that the permissible CFL number of the present solver is up to unity while that of the one-dimensional HLLEM solver can not be more than 0.5. The present solver is easy to implement and is promising to be applied to numerical simulations of compressible flows that involve complex flow phenomena, such as strong shock waves, shock-shock interactions and shear layers.

Declaration of Competing Interest

The authors declare that they have no known competing financial interests or personal relationships that could have appeared to influence the work reported in this paper.

CRediT authorship contribution statement

Lijun Hu: Conceptualization, Methodology, Writing - original draft. **Li Yuan:** Writing - review & editing. **Kunlei Zhao:** Validation.

Acknowledgements

This work was supported by the [National Natural Science Foundation of China](#) (91641107, 91852116). The constructive comments of the anonymous reviewers are gratefully acknowledged.

References

- [1] Roe PL. Approximate Riemann solvers, parameter vectors, and difference schemes. *J Comput Phys* 1981;43:357–72.
- [2] Harten A, Lax PD, van Leer B. On upstream differencing and Godunov-type schemes for hyperbolic conservation laws. *SIAM Rev* 1983;25:35–61.
- [3] Einfeldt B. On Godunov-type methods for gas dynamics. *SIAM J Numer Anal* 1988;25:294–318.
- [4] Einfeldt B, Munz C-D, Roe PL, Sjögren B. On Godunov-type methods near low densities. *J Comput Phys* 1991;92:273–95.
- [5] Toro EF, Spruce M, Speares W. Restoration of the contact surface in the HLL-riemann solver. *Shock Waves* 1994;4:25–34.
- [6] Liou MS. A sequel to AUSM: AUSM+. *J Comput Phys* 1996;129:364–82.
- [7] Kim KH, Kim C, Rho OH. Methods for the accurate computations of hypersonic flows i: AUSMPP+ scheme. *J Comput Phys* 2001;174:38–80.
- [8] Liou MS. A sequel to AUSM, part II: AUSM+-up for all speeds. *J Comput Phys* 2006;214:137–70.
- [9] Qu F, Sun D, Yan C. A new flux splitting scheme for the euler equations II: E-AUSMPPWAS for all speeds. *Commun Nonlinear Sci Numer Simul* 2018;57:58–79.
- [10] Simon S, Mandal JC. A cure for numerical shock instability in HLLC Riemann solver using antidiffusion control. *Comput Fluids* 2018;174:144–66.
- [11] Mandal JC, Panwar V. Robust HLL-type Riemann solver capable of resolving contact discontinuity. *Comput Fluids* 2012;63:148–64.
- [12] Xie W, Li W, Li H. On numerical instabilities of Godunov-type schemes for strong shocks. *J Comput Phys* 2017;350:607–37.
- [13] Park SH, Kwon JH. On the dissipation mechanism of Godunov-type schemes. *J Comput Phys* 2003;188:524–42.
- [14] Dumbser M, Balsara DS. A new efficient formulation of the HLLEM Riemann solver for general conservative and non-conservative hyperbolic systems. *J Comput Phys* 2016;304:275–319.
- [15] Quirk JJ. A contribution to the great Riemann solver debate. *Int J Numer Methods Fluids* 1994;18:555–74.
- [16] Kim SD, Lee BJ, Lee HJ, Jeung IS. Robust HLLC Riemann solver with weighted average flux scheme for strong shock. *J Comput Phys* 2009;228:7634–42.
- [17] Huang K, Wu H, Yu H, Yan D. Cures for numerical shock instability in HLLC solver. *Int J Numer Methods Fluids* 2011;65:1026–38.
- [18] Hu L, Yuan L. Analysis of numerical shock instability and a hybrid curing method. *Appl Math Mech Chin Ed* 2015;36:482–93.
- [19] Simon S, Mandal JC. A simple cure for numerical shock instability in the HLLC Riemann solver. *J Comput Phys* 2019;378:477–96.
- [20] Rodionov AV. Artificial viscosity in Godunov-type schemes to cure the carbuncle phenomenon. *J Comput Phys* 2017;345:308–29.
- [21] Rodionov AV. Artificial viscosity to cure the shock instability in high-order Godunov-type schemes. *Comput Fluids* 2019;190:77–97.
- [22] Chen S, Yan C, Lin B. Affordable shock-stable item for Godunov-type schemes against carbuncle phenomenon. *J Comput Phys* 2018;373:662–72.
- [23] Chen Z, Huang X, Ren Y-X, Zhou M. General procedure for Riemann solver to eliminate carbuncle and shock instability. *AIAA J* 2017;55:2002–15.
- [24] Collela P. Multidimensional upwind methods for hyperbolic conservation laws. *J Comput Phys* 1990;87:171–200.
- [25] Brio M, Zakharian AR, Webb GM. Two dimensional Riemann solver for euler equations for gas dynamics. *J Comput Phys* 2001;167:177–95.
- [26] Rumsey CL, van Leer B, Roe PL. A multidimensional flux function with application to the euler and Navier-Stokes equations. *J Comput Phys* 1993;105:306–23.
- [27] Saltzman J. An unsplit 3d upwind method for hyperbolic conservation laws. *J Comput Phys* 1994;115:153–68.
- [28] LeVeque RJ. Wave propagation algorithms for multi-dimensional hyperbolic systems. *J Comput Phys* 1997;131:327–53.
- [29] Billet SJ, Toro EF. On WAF-type schemes for multidimensional hyperbolic conservation laws. *J Comput Phys* 1997;130:1–24.
- [30] Wendroff B. A two-dimensional HLLC Riemann solver and associated Godunov-type difference scheme for gas dynamics. *Comput Math Appl* 1999;38:175–85.
- [31] Fey M. Multidimensional upwinding. Part I. The method of transport for solving the euler equations. *J Comput Phys* 1998;143:159–80.
- [32] Balsara DS. Multidimensional HLLC Riemann solver: application to euler and magnetohydrodynamic flows. *J Comput Phys* 2010;229:1970–93.
- [33] Balsara DS. Three dimensional HLL Riemann solver for conservation laws on structured meshes; application to euler and magnetohydrodynamic flows. *J Comput Phys* 2015;295:1–23.
- [34] Balsara DS. A two-dimensional HLLC Riemann solver for conservation laws: application to euler and magnetohydrodynamic flows. *J Comput Phys* 2012;231:7476–503.
- [35] Balsara DS. Multidimensional Riemann problem with self-similar internal structure. Part I-application to hyperbolic conservation laws on structured meshes. *J Comput Phys* 2014;277:163–200.
- [36] Balsara DS, Dumbser M. Multidimensional Riemann problem with self-similar internal structure. Part II-application to hyperbolic conservation laws on unstructured meshes. *J Comput Phys* 2015;287:269–92.
- [37] Gallardo JM, Schneider KA, Castro MJ. On a class of two-dimensional incomplete Riemann solvers. *J Comput Phys* 2019;386:541–67.
- [38] Zha G-C, Bilgen E. Numerical solutions of euler equations by using a new flux vector splitting scheme. *Int J Numer Methods Fluids* 1993;17:115–44.

- [39] Mandal JC, Sharma V. A genuinely multidimensional convective-pressure flux split Riemann solver for euler equations. *J Comput Phys* 2015;297:669–88.
- [40] Qu F, Sun D, Bai J. A new genuinely two-dimensional Riemann solver for multidimensional Euler and Navier-Stokes equations. *Comput Phys Commun* 2019;243:1–11.
- [41] Hu L, Yuan L. A genuinely multidimensional Riemann solver based on the TV splitting. *Appl Math Mech Chin Ed* 2017;38:243–64.
- [42] Qu F, Sun D, Bai J, Yan C. A genuinely two-dimensional Riemann solver for compressible flows in curvilinear coordinates. *J Comput Phys* 2019;386:47–63.
- [43] Gressier J, Moschetta JM. Robustness versus accuracy in shock-wave computations. *Int J Numer Methods Fluids* 2000;33:313–32.
- [44] Dumbser M, Moschetta J-M, Gressier J. A matrix stability analysis of the carbuncle phenomenon. *J Comput Phys* 2004;197:647–70.
- [45] Kemm F. Heuristical and numerical considerations for the carbuncle phenomenon. *Appl Math Comput* 2018;320:596–613.
- [46] Mandal JC, Arvind N. High resolution schemes for genuinely two-dimensional HLL Riemann solver. *Prog Comput Fluid Dy* 2014;14:205–20.
- [47] Simon S, Mandal JC. Strategies to cure numerical shock instability in the HLLM Riemann solver. *Int J Numer Methods Fluids* 2019;89:533–69.
- [48] Woodward P, Colella P. The numerical simulation of two-dimensional fluid flow with strong shocks. *J Comput Phys* 1984;54:115–73.
- [49] San O, Kara K. Numerical assessments of high-order accurate shock capturing schemes: Kelvin-Helmholtz type vortical structures in high-resolutions. *Comput Fluids* 2014;89:254–76.